

NUCLEAR-RESONANCE EXCITATION IN  $F^{19}$  AND  $Mn^{55}$  WITH A  
GERMANIUM BENT-CRYSTAL MONOCHROMATOR

Thesis by

Edward Joseph Seppi

In Partial Fulfillment of the Requirements

For the Degree of

Doctor of Philosophy

California Institute of Technology

Pasadena, California

1962

## ACKNOWLEDGEMENTS

The nuclear-resonance excitation-experiments reported in this thesis were originally conceived and initiated by Professor Felix Boehm. I would like to thank him for introducing me to the problem and for his supervision and encouragement during the entire course of my research.

I wish to express my appreciation to Professor J. W. M. DuMond for his constant interest in the progress of my research and for his valuable advice and encouragement.

Mr. Herbert Henrikson is responsible for the design and construction of the monochromator described in this thesis. The excellent precision of the instrument is a direct result of his work.

I wish to thank Mr. C. H. Holland and Mr. D. Agresti for their assistance in collection and analysis of the data. I would also like to express my appreciation for my scientific association with other members of the physics research group.

I gratefully acknowledge the financial aid given me by the California Institute of Technology and by the General Electric Foundation.

Finally, I wish to thank my wife, Betty, who contributed in many ways to the successful completion of this work.

## ABSTRACT

A precision bent-crystal gamma-ray monochromator with stationary source has been built. The instrument consists of three physically independent units: The line source (a radioactive source or the anode of an x-ray tube), the two-meter-radius bent-diffraction-crystal with its pivot and sine-motion mechanism, and the heavy-duty curved-track framework which supports the collimator, detector, and shielding. The motions of the crystal-pivot unit and of the detector-carriage unit are linked together in such a way that the reflection condition is satisfied.

Results are presented showing that the precision of the monochromator for measurement of gamma-ray wavelengths is 0.003 x-units. The line width at half-maximum observed when the (800) planes of a bent germanium-crystal are used is 0.080 x-units. The resolution which has been attained with the germanium crystal is illustrated by a measurement of the 244.264 keV, 246.056 keV, and the previously unobserved 245.237 keV gamma line in the decay of  $W^{183}$ .

Nuclear-resonance scattering from the first-excited states in  $F^{19}$  and  $Mn^{55}$  has been observed with the bent-diffraction-crystal monochromator. The experiment was performed by observing the scattered radiation from nuclei exposed to nearly monoenergetic x-rays selected by crystal diffraction from the bremsstrahlung spectrum of an x-ray tube. Gamma rays scattered at  $135^\circ$  from samples of lithium fluoride and manganese placed in the diffracted beam were observed as a function of the incident photon wavelength. With the lithium fluoride sample three measurements were made under different experimental conditions. In each case pronounced resonance peaks 10 to 15 percent above background were observed. A least-square analysis of the data gives  $109.894 \pm 0.005$  keV for the energy position of the first-excited level in  $F^{19}$ . From the observed yield the width of this level was deduced to be  $(5.1 \pm 0.7)10^{-7}$  eV. Measurements with a  $Mn^{55}$  scattering sample gave  $125.95 \pm 0.01$  keV for the position of the first-excited level and  $(1.1 \pm 0.3)10^{-6}$  eV for the resonance width.

NUCLEAR-RESONANCE EXCITATION IN  $F^{19}$  AND  $Mn^{55}$  WITH A  
GERMANIUM BENT-CRYSTAL MONOCHROMATOR

Table of Contents

Acknowledgements

Abstract

Table of Contents

Part One: The Germanium Bent-Crystal Monochromator. . . . .	1
I. Introduction . . . . .	2
II. Design of the Monochromator. . . . .	3
A. Description of the Crystal Pivot and the Detector Carriage	3
B. Description of the Diffraction Crystals and Crystal Holder	6
III. Monochromator Wavelength Calibration . . . . .	8
A. Gage Block Calibration . . . . .	8
B. Gamma-Line Wavelength Calibration. . . . .	8
IV. Monochromator Resolution and Reflection Power. . . . .	14
V. Example of the Performance of the Monochromator: a new line observed in decay of $W^{183}$ . . . . .	18
Part Two: Nuclear-Resonance Excitation in $F^{19}$ and $Mn^{55}$ . . . . .	23
I. Introduction . . . . .	24
II. Interactions of Electromagnetic Radiation With Matter. . . . .	29
A. Cross Sections for Nuclear Resonance Excitation. . . . .	30
B. Crystal Binding and Doppler Effects. . . . .	31
C. Cross Section for Compton Scattering . . . . .	34

-Continued-  
Table of Contents

III. Description of the Experiment. . . . .	36
A. Formula for the Experimental Determination of Resonance Width. . . . .	38
B. Results of the Experiments With a Lithium Fluoride Scattering Sample. . . . .	42
C. Results of the Experiments With a Manganese Scattering Sample . . . . .	53
IV. Final Results and Conclusions. . . . .	56
Appendix I. Mechanical Design of the Monochromator. . . . .	60
A. Design of the Crystal-Pivot Unit . . . . .	60
B. Design of the Detector Carriage. . . . .	66
Appendix II. Determination of Nuclear Resonance Width Using a Scattering Sample of Arbitrary Thickness . . . . .	68
Appendix III. Corrections Applied to Managanese and Fluorine Data .	73
Appendix IV. Analysis of the Intensities Observed in the Elastic and Inelastic Counting Channels. . . . .	76
Appendix V. Correction for Rayleigh Scattering Effects in the Manganese Experiment. . . . .	79
References . . . . .	84

PART ONE

THE GERMANIUM BENT-CRYSTAL MONOCHROMATOR

## I. INTRODUCTION

Curved-crystal diffraction monochromators and spectrometers have been described by several authors. A review article including a complete list of references has been written by DuMond (1). The instruments make use of the focusing Bragg-reflection property of a curved crystal, such as quartz. In the monochromator arrangement the line-shaped source is situated on the focal circle through the curved crystal. Gamma-rays scattered at the Bragg angle are detected by a large NaI counter after having passed through a collimator. The monochromator has considerably higher luminosity, per unit wavelength interval, as compared to the spectrometer arrangement in which the role of the source and counter is interchanged. It is, therefore, well suited for experiments where gamma-ray or x-ray lines are scanned in a point-by-point manner over a certain wavelength interval.

The California Institute of Technology monochromator (Mark I) built by DuMond (1, 2, 3) uses a stationary collimator and detector system. Both source and crystal move in such a fashion that the Bragg condition is maintained at all times. For many applications, however, it is desirable to have a stationary source, for example, if the source is connected to a reactor, an accelerator, or an x-ray tube.

The instrument described in this paper is a monochromator with stationary source. It has been primarily designed for nuclear-resonance scattering-experiments using a powerful x-ray tube. It also is being used as a precision wavelength measuring device. It has an accuracy somewhat superior to Mark I.

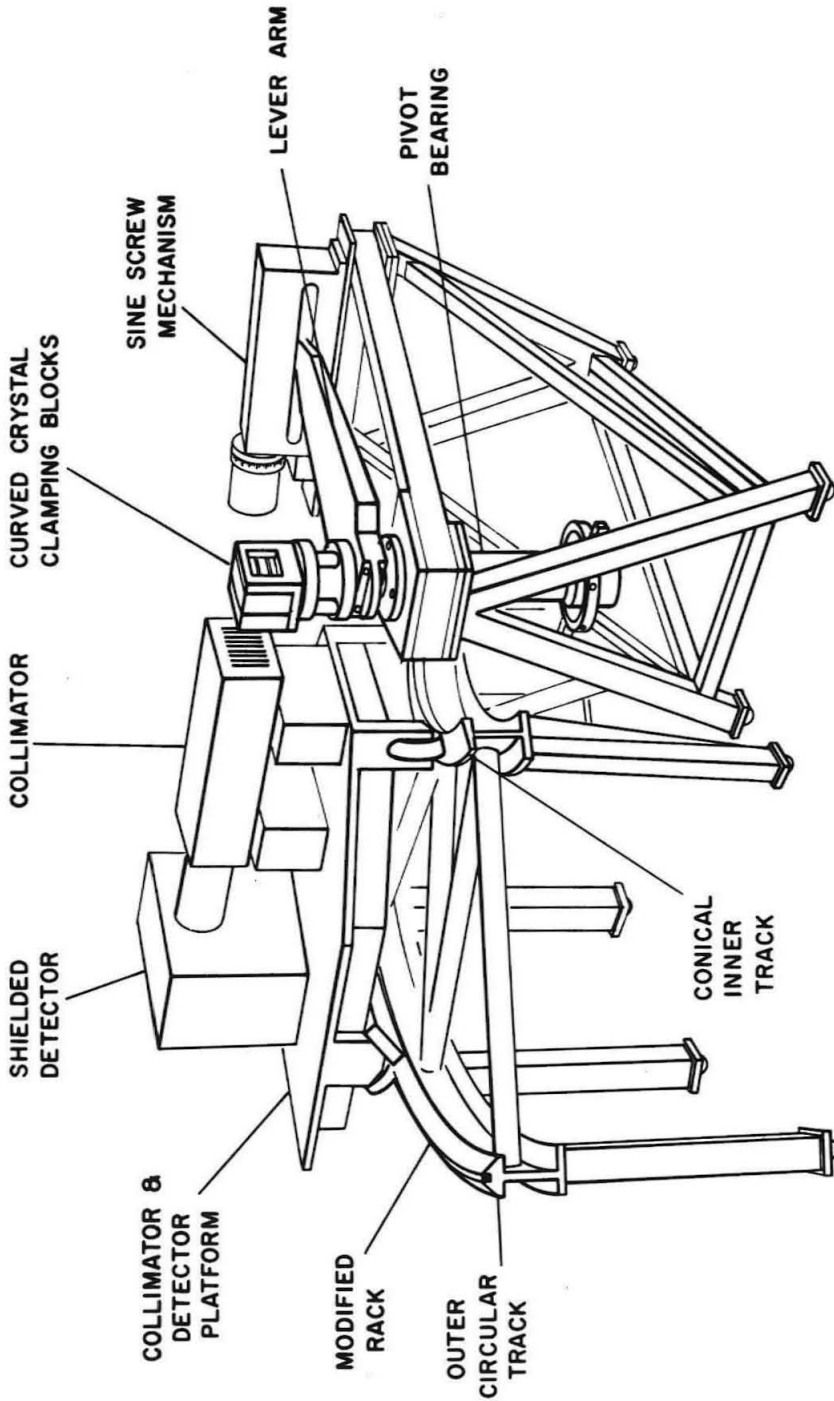
## II. DESIGN OF THE MONOCHROMATOR

### A. Description of the Crystal Pivot and the Detector Carriage

The monochromator consists of three physically independent units: (i) the crystal pivot, (ii) the detector carriage, and (iii) the line source (a radioactive source or the anode of an x-ray tube). The crystal-pivot and detector-carriage units are illustrated by a line drawing in Fig. 1. A photograph of the crystal pivot is shown in Fig. 2. In this section we will present a brief description of these two units and refer the reader to Appendix I for a detailed description of the mechanical design.

The crystal-pivot unit (Fig. 1) contains the bent-diffraction crystal, the pivot bearing, and the precision sine-screw mechanism. The precision lead screw moves the lever arm which turns the diffraction crystal about an axis provided by the pivot bearing. The sine of the Bragg angle is determined through the sine-screw mechanism and can be read off directly on a dial. This reading is, of course, directly proportional to the wavelength. The design is such that on the monochromator dial the "screw division"(s.d.) corresponds to one x-unit when the diffraction is from the (310) planes of quartz. Included in the sine-screw mechanism is a calibration cam which is used to correct for small non-linearities in the pitch of the lead screw.

The detector-carriage unit (Fig. 1) provides for the motion of the heavily shielded detector and collimator system in such a way that the Bragg reflection condition is satisfied. The shielded detector and



DETECTOR CARRIAGE      CRYSTAL PIVOT

DETECTOR CARRIAGE      CRYSTAL PIVOT

Fig. 1. Line drawing of the bent-crystal monochromator illustrating the crystal-pivot unit and the detector-carriage unit.

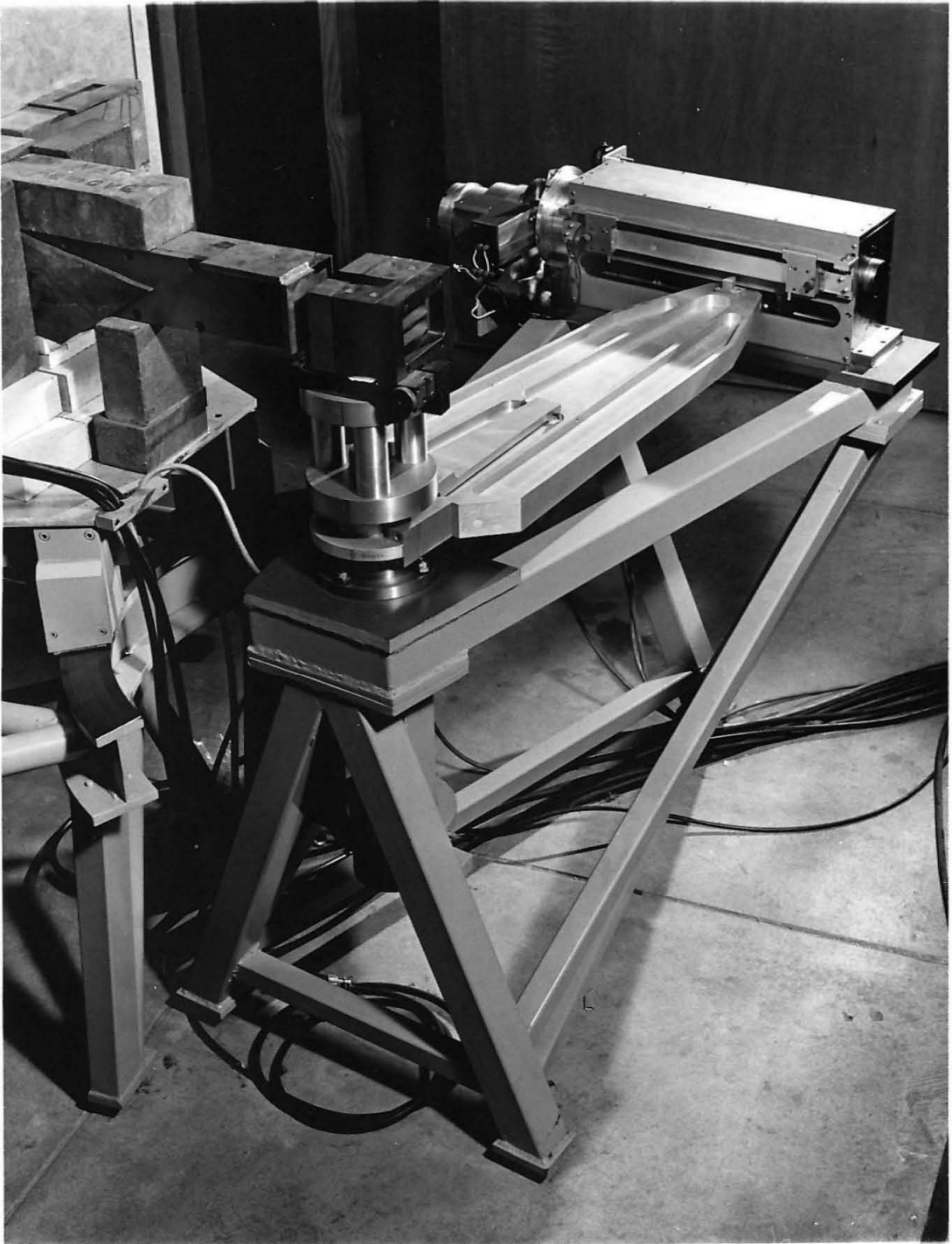


Fig. 2. A photograph of the monochromator crystal-pivot unit showing the curved-crystal clamping-blocks, the pivot bearings, the lever arm, and the sine-screw mechanism.

collimator are carried on a platform which is constrained by circular tracks to rotate about an axis through the pivot bearing. The motion of the platform is electrically linked to that of the crystal pivot. The design of the detector carriage as a unit mechanically separate from the crystal pivot has the advantage that mechanical strains resulting from the motion of the heavy shielding have no effect on the precise crystal setting which is determined by the sine-screw mechanism.

#### B. Description of the Diffraction Crystals and Crystal Holder

The Bragg reflection is provided by a thin optically ground lamina of quartz or germanium clamped between stainless steel blocks which have been profiled to a two-meter radius of curvature. The single crystals are oriented so that the quartz (310) and germanium (400) planes are used in the reflection. The quartz crystal is a square lamina 7.5 cm by 7.5 cm and 2 mm thick. Excellent results have been achieved in the energy resolution and reflection power obtained using the germanium crystal. The germanium crystal is a rectangular lamina 7.5 cm by 3.8 cm and 1.3 mm thick. The crystal slab was cut from an oriented cylindrical single crystal ingot of germanium\*. Before bending, the dislocation density of the crystal was less than 5,000 pits/cm<sup>2</sup>. The slab was optically polished on both sides to a flatness of about 10 fringes of sodium light and then mounted in the crystal clamping-

---

\* The crystal slab was prepared by Mono Silicon, Inc., Gardena, California, under the direction of Dr. Simon A. Prussin.

blocks described below. This crystal is smaller than the optimum size and will be replaced with a larger one as soon as larger ingots become available.

The method developed by DuMond, Lind, and Cohen (4) is used to grind the concave and convex cylindrical surfaces of the clamping blocks. The blocks have a 5.5 x 4.5 cm aperture. The convex-block aperture has two ribs running normal to the generators of the cylinder. The surface of this block is lapped against the mating concave surface of a cast iron block which has been checked by the Foucault knife-edge test and corrected to better than one quarter of a fringe of sodium light.

The microscopic scratches in the surface and edges of the quartz lamina present a danger when the crystal is being bent. To minimize the possibility of fracture the quartz is etched with concentrated hydrofluoric acid. The scratches are etched preferentially eliminating the sharp V character of the grooves. No treatment was applied to the germanium crystal before bending.

The crystal bending is done in a dust-free box. For the quartz crystal, optical contact is checked by observing the interference fringes in the interface between the crystal lamina and the convex surface of the clamping block. A thin neoprene gasket (0.5 mm) is placed on the crystal; then the concave block is slowly clamped in place with four spring-loaded screws. When bending a germanium-crystal lamina, interference fringes cannot, of course, be observed; therefore great caution must be exercised to insure a dust free

interface. When finally clamped in place the concave surface of the germanium can be checked with the Foucault knife-edge test to verify its conforming to the convex crystal clamping block.

### III. MONOCHROMATOR WAVELENGTH CALIBRATION

#### A. Gage Block Calibration

In the initial wavelength calibration of the monochromator, precision gage blocks were used to determine the linearity of the monochromator screw. The calibration cam described in the section on the crystal pivot in Appendix I is used to correct for small deviations in the linearity of the precision ground and lapped screw. The calibration curve A shown in Fig. 3 is obtained when a linear cam is used. The curve shows the deviation in the screw position from that measured by gage blocks as a function of the position on the screw. Scales on the figure show the measured dimensions in inches and also in screw divisions. Curve B of Fig. 3 shows a calibration measurement using a cam profiled to correct for the deviations shown on curve A. For the curve B the RMS deviation of the points from linearity is 0.002 s.d. Data points are not shown in the region +200 to +400 s.d. In this region an error was discovered which required a change in the shape of the calibration cam. A new cam was installed which now results in an overall linear monochromator setting to within the accuracy shown on the curve B.

#### B. Gamma-Line Wavelength Calibration

A check on the final calibration has been made by measurements of several gamma lines using germanium and quartz diffraction crystals.

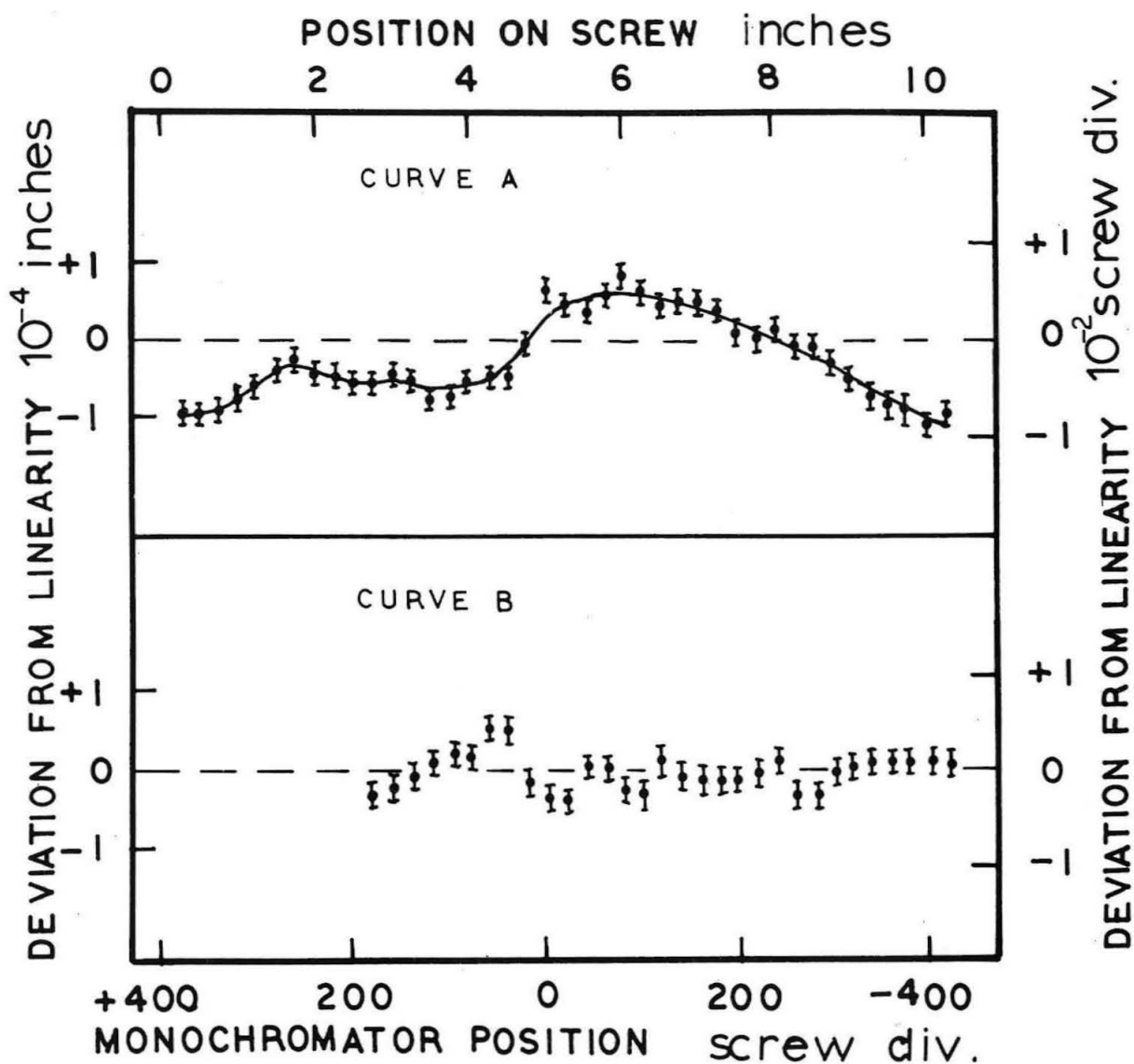


Fig. 3. Calibration curves giving the deviation of the screw position from linearity versus the monochromator position. Curve A was obtained with a linear calibration cam. Curve B was obtained using a cam profiled to correct for the deviations shown in curve A.

Consistency checks have been made in two ways: (i) by comparing the measured wavelengths of a single gamma line in various orders,  $n$ , of reflection from the germanium crystal and in first order from the quartz, (ii) by making use of certain well-established gamma-ray energy-combination equations known from the decay schemes.

With these two methods interrelated measurements are possible covering the entire range of the monochromator and an overall linearity check has been established. In this section the results of the consistency check (i) are analyzed to determine a formula for estimating the error of the wavelength measurements. Errors calculated using the derived formula are then compared with the deviations observed in the consistency check (ii). Finally possible sources of monochromator error are examined.

For the calibration investigation gamma lines from the well-known decay of  $Ta^{182}$  and  $Ta^{183}$  were used. The gamma decay schemes of these isotopes have been established by Murray, Boehm, Marmier, and DuMond (5). These two isotopes supply intense gamma lines over a considerable portion of the useful energy range of the monochromator. Using standard techniques (2) a 0.005 inch diameter tantalum wire was irradiated at the Material Testing Reactor in Arco, Idaho. With this source the wavelength results listed in Table I were obtained. Also listed in the table are the results of Murray, et al. (5) which were obtained with the Mark I instrument.

The errors  $\epsilon$  listed in Table I were obtained from the formulas

$$\epsilon^2 = \epsilon_c^2 + \epsilon_m^2, \quad \epsilon_m = 0.003 \text{ s.d.} \quad (1)$$



where the standard deviation  $\epsilon_c$  is the error in the position of the gamma line resulting from the statistical counting error in the data. The monochromator error  $\epsilon_m$  represents the non-statistical part of the error and gives an indication of the overall reproducibility and self-consistency of the instrument. The monochromator error is a measured quantity which was determined from the data in Table I through the formula

$$\epsilon_m^2 = \frac{\sum_{ij} [(\lambda^{ij} - \lambda_{ave}^j)n]^2 - [n\epsilon_c^{ij}]^2}{N - 1} \quad (2)$$

where  $n$  is the order of the reflection and  $\lambda_{ave}^j$  is the average wavelength found for the group of measurements of the gamma line  $j$ . The symbols  $\lambda^{ij}$  and  $\epsilon_c^{ij}$  represent respectively the observed wavelength and statistical counting error of the  $i^{th}$  measurement of the line  $j$ . In the sum three or more independent measurements labelled  $i$  were taken from columns I to VI of Table I of the following gamma-rays; FD, BA, KG, in  $W^{182}$  and DC, EB, GC, IE, ID, IC in  $W^{183}$ . The total number  $N$  of points summed was 32. From this procedure the value of  $\epsilon_m$  was found to be equal to 0.003 s.d.

Making use of the gamma-ray energy combination-equations known from the decay schemes of  $W^{182}$  and  $W^{183}$  a check has been made on the magnitude of  $\epsilon_m$  in Eq. 1. The combination equations are given in column I and II of Table II. A list of the observed values of the left (column I) and right (column II) sides of the combination equations is presented in columns III and IV respectively. The statistical consistency of the

TABLE II. Energy combination equations for tungsten 182 and tungsten 183.

Combination Equation		Observed Values for Column I	Observed Values for Column II
I	II	III	IV
Tungsten 182			
KJ + JF	= KF	264.079 ± 0.005	264.075 ± 0.009
KJ + JG	= KG	222.109 ± 0.003	222.114 ± 0.004
JH + HF	= JF	198.367 ± 0.002	198.356 ± 0.005
KJ + JH	= KH	179.397 ± 0.002	179.394 ± 0.004
HF + FD	= HD	152.444 ± 0.001	152.441 ± 0.003
Tungsten 183			
ID + DC	= IC	353.989 ± 0.002	354.004 ± 0.010
ID + DC + CB	= IE + EB	406.587 ± 0.002	406.587 ± 0.006

deviations between the values in columns III and IV and the errors listed represents a check on the magnitude of  $\epsilon_m$ . Based on the results of the two methods of checking the wavelength calibration we conclude that the error in the monochromator is given by Eq. 1 with the value of  $\epsilon_m$  equal to 0.003 s.d.

Monochromator errors which contribute to the overall error  $\epsilon_m$  result from (i) screw non-linearity, (ii) lack of complete reproducibility of settings, and (iii) deviations caused by temperature variations. The contribution from screw non-linearity is found to be less than 0.002 s.d. as measured with gage blocks. No deviations have been measured which can be attributed to a lack of reproducibility of monochromator settings. Deviations due to temperature variations can contribute significantly to the error of the monochromator reading. The temperature coefficient due to the thermal expansion of the mechanical parts of the monochromator is estimated to be  $-(5 \text{ to } 13)10^{-6} \lambda$  s.d. per  $^{\circ}\text{C}$  where  $\lambda$  is the monochromator setting in screw divisions. The temperature coefficient (6) due to the expansion of the diffraction crystal is  $10.4 \times 10^{-6} \lambda$  s.d. per  $^{\circ}\text{C}$  for the quartz crystal and  $6.9 \times 10^{-6} \lambda$  s.d. per  $^{\circ}\text{C}$  for the germanium crystal. The variation of room temperature during the accumulation of data in Table I was less than  $3^{\circ}\text{C}$ . The error due to temperature variations is thus comparable to the error from screw non-linearity.

#### IV. MONOCHROMATOR RESOLUTION AND REFLECTION POWER

Use of the germanium diffraction crystal in place of the quartz crystal gives considerable improvement in the resolution and intensity

obtained with the monochromator. The higher order-reflections of the germanium (400) n planes provide sufficient intensity to be useful for high resolution measurements. The best resolution we have obtained was achieved with a 0.002 inch diameter tantalum wire source. For this source the full width at one-half maximum of the gamma lines in W<sup>182</sup> and W<sup>183</sup> is

$$\Delta \lambda = \frac{0.16}{n} \text{ x-units, or } \Delta E = 1.3 \times 10^{-5} \frac{E^2}{n} \text{ kev} \quad (3)$$

where E is the energy in kev and n is the order of reflection. Some results obtained with this source are presented in Chapter V.

In an attempt to better understand the reflectivity laws of the germanium crystal, measurements of gamma lines were made in various orders of reflection. The results have been analyzed by a least-square fit to an equation based on the assumption (7) of a mosaic crystal. With this assumption it can be shown (8) that neglecting the atomic absorption the reflectivity R(E, n) is approximately given by

$$R(E, n) = \int_{-\Delta}^{+\Delta} \left[ 1 - e^{-2M(\mathcal{J})R_H} \right] \frac{d\mathcal{J}}{4\Delta} \quad (4)$$

where M( $\mathcal{J}$ ) is a Gaussian with a half-width given by the crystal mosaic. The range of the integration,  $2\Delta$ , is the angle projected at the crystal by the source. The function  $R_H$  is given by

$$R_H = \underline{d}_H \lambda^2 (fF_H/V)^2 t e^{-2W(\Theta)} \quad (5)$$

where  $\underline{d}_H$  is the lattice spacing, V is the volume of the unit cell,

t is the thickness of the crystal, f is the atomic scattering power (9),  $F_H$  is the lattice structure factor, and  $e^{-2W(\Theta)}$  is the Debye factor which is a function of the Debye temperature  $\Theta$ . In the limit of a thin crystal and a narrow source the energy dependence of the reflectivity (Eq. 4) approaches the well-known  $E^{-2}$  law (7, 10).

Experimentally we have determined the ratio of the reflectivity for an energy E in the  $n^{\text{th}}$  order to that for energy  $E_0$  in the  $n_0^{\text{th}}$  order. The experiment furnishes this ratio in the following way:

$$\frac{R(E,n)}{R(E_0,n_0)} = \frac{I(E,n)}{I(E_0,n_0)} \cdot \frac{T(E_0)}{T(E)} \cdot \frac{I_\gamma(E_0)}{I_\gamma(E)} \cdot \frac{\epsilon(E_0)}{\epsilon(E)} \quad (6)$$

where  $I(E,n)/I(E_0,n_0)$  is the observed ratio of counts in the detector,  $T(E)$  is the transmission through the crystal derived from the atomic absorption coefficient,  $I_\gamma(E)$  is the intensity of the gamma line as measured by Edwards (11), and  $\epsilon(E)$  is the efficiency of the detector (including air and source absorption). The values of  $I(E,n)$  were measured for several tungsten lines. Ratios were then determined from Eq. 6 with  $n_0$  equal to one and with  $E_0$  equal to 100.107 kev and 107.933 kev, respectively, for gamma lines in  $W^{182}$  and  $W^{183}$ . These ratios have been plotted in Fig. 4.

A least-square fit was made of the observed ratios to those calculated through Eq. 4 with the crystal mosaic width and the Debye temperature as the variable parameters. The curves shown in Fig. 4 were calculated based on the values 7.5 seconds for the mosaic width and 275°K for the Debye temperature which were determined through the least-square analysis. The crystal thickness was 1.3 mm. The

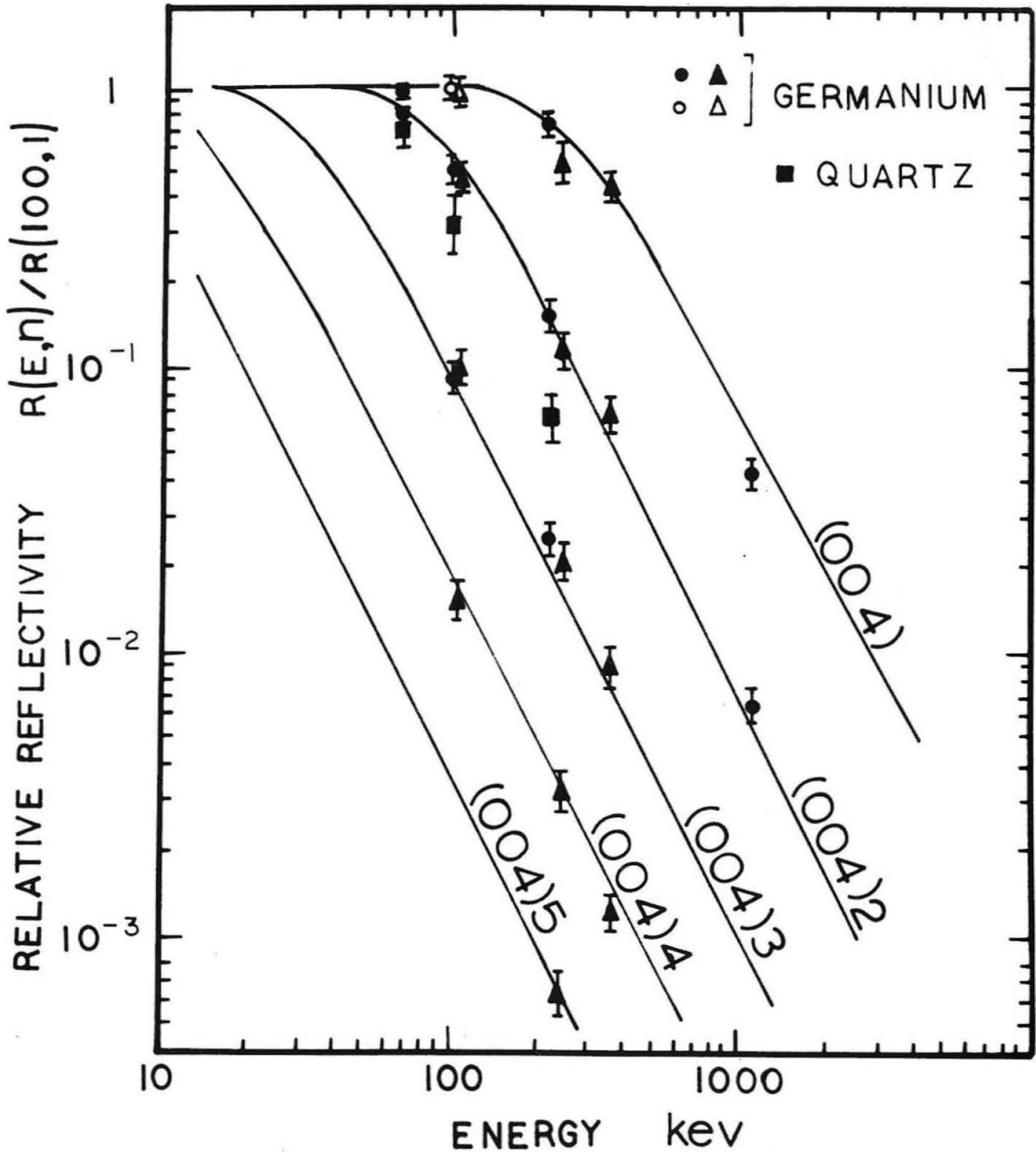


Fig. 4. Relative reflectivity of the germanium and quartz crystals versus gamma-ray energy. Based on Eq. 6 data points giving the observed relative reflectivity from the germanium (400) planes in various orders are shown as circular and triangular points for gamma lines in  $W^{182}$  and  $W^{183}$ , respectively. The data points are normalized to 1.0 for the first-order reflection of the gamma lines at 100.107 keV and 107.933 keV (hollow points). The curves show results obtained using Eq. 4 in a least-square fit to the germanium-reflectivity data. The solid square points represent the reflectivity of the quartz crystal relative to the germanium crystal.

calculated curves and observed data points are in agreement to within the estimated accuracy of the data. It is of interest to conclude from this that Eq. 4 based on a mosaic crystal seems to account for the experimental findings.

We have also compared the reflectivity of our germanium-crystal (400) planes to that of our quartz-crystal (310) planes. The ratio of the monochromator counting rate with the germanium crystal to the counting rate with the quartz crystal was observed for several gamma lines of  $W^{182}$ . The observed ratio was multiplied by 1.5 to account for the differences in the areas of the crystals. The ratios  $I_{Ge}/I_{SiO_2}$  are given in Table III. (The thickness of the two crystals is given in Chapter II.) The ratio of the reflectivities  $R_{Ge}/R_{SiO_2}$  presented in Table III is equal to the product of  $I_{Ge}/I_{SiO_2}$  and the ratio of the crystal transmissions  $T^{SiO_2}(E)/T^{Ge}(E)$ . For a graphic comparison of the reflectivities the values of the quantity  $(R^{SiO_2}/R^{Ge}) R(E,n)/R(100,1)$  for the three gamma energies are shown as solid squares in Fig. 4.

#### V. PERFORMANCE OF THE MONOCHROMATOR:

##### A New Line Observed in Decay of $W^{183}$

In the decay scheme of  $W^{183}$ , Murray et al. (5) predicted the transition FB (see Table I) with an energy of 245.23 kev. This transition has not previously been observed because of the existence of the transitions with energy 246.056 and 244.264 in  $W^{183}$  both of which are considerably more intense than the 245.23 kev transition.

TABLE III. Comparison of reflection from germanium and from quartz.\*

Gamma-Ray Energy kev	$I_{\text{Ge}}/I_{\text{SiO}_2}$	$R_{\text{Ge}}/R_{\text{SiO}_2}$
67.751	$0.6 \pm 0.1$	$1.4 \pm 0.2$
100.107	$2.4 \pm 0.6$	$3.1 \pm 0.8$
222.114	$11.1 \pm 2.3$	$11.5 \pm 2.4$

\*  $I_{\text{Ge}}/I_{\text{SiO}_2}$  is equal to the observed ratio of counts multiplied by 1.5 to account for the differences in areas of the crystals.  
 $R_{\text{Ge}}/R_{\text{SiO}_2}$  is the ratio of the reflectivities.

We have looked for this line with the present instrument. The source used in the measurement was a 0.002 inch tantalum wire. Figure 5 shows the results which were obtained. The 245.23 kev transition is well resolved between the lines at 246.056 and 244.264 kev. Shown in Fig. 6, for comparison, are results which were obtained with the quartz crystal with a standard 0.008 inch diameter source. From a least-square analysis of the data the ratio of the intensity of the 245.24 kev line to that of the 246.056 kev line was found to be  $(1.15 \pm 0.03)10^{-2}$  and the energy of the transition was determined to be  $245.237 \pm 0.008$  kev.

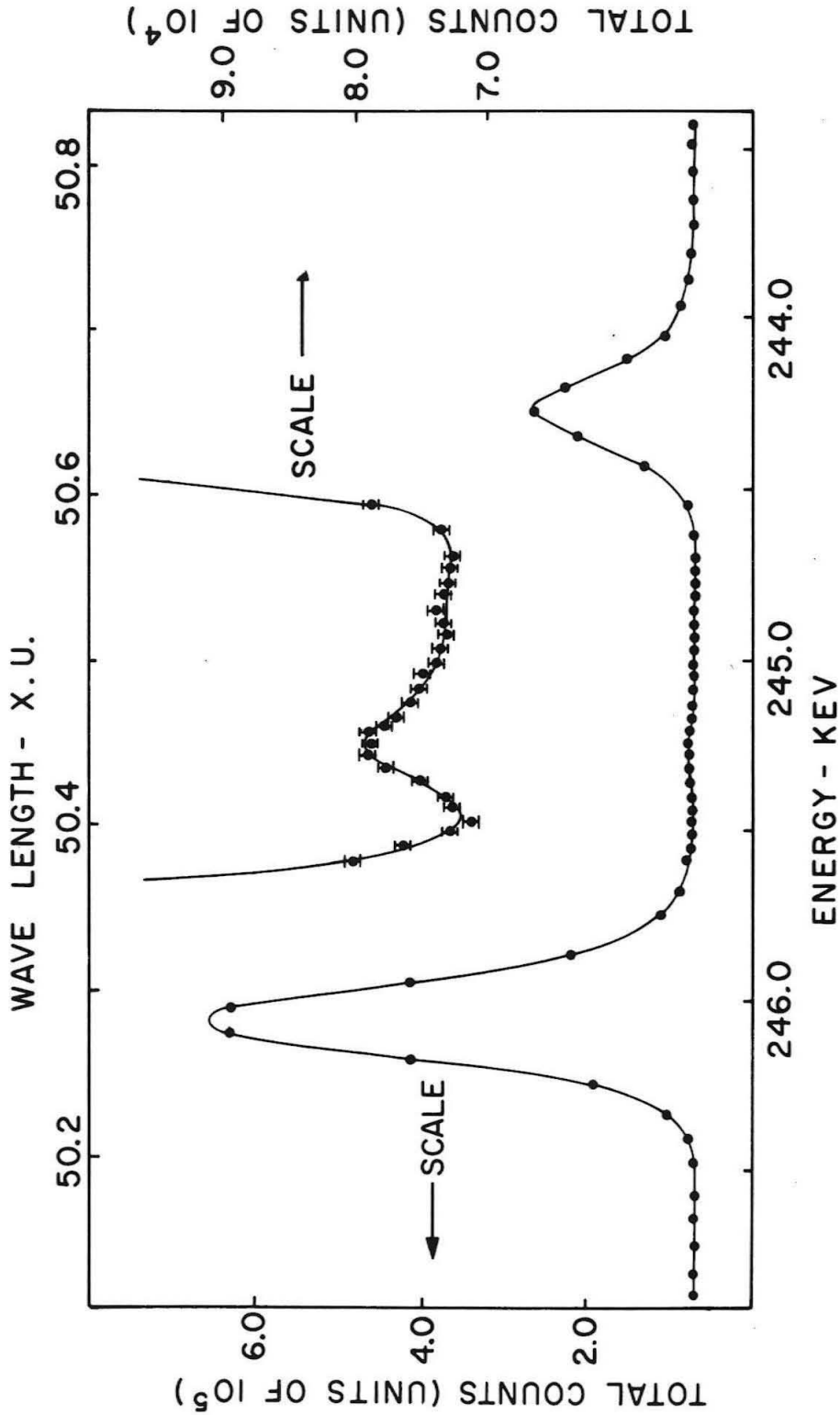


Fig. 5. The 246.056, 245.237, and 244.264 keV gamma-ray lines in W183 observed in third-order reflection from germanium.

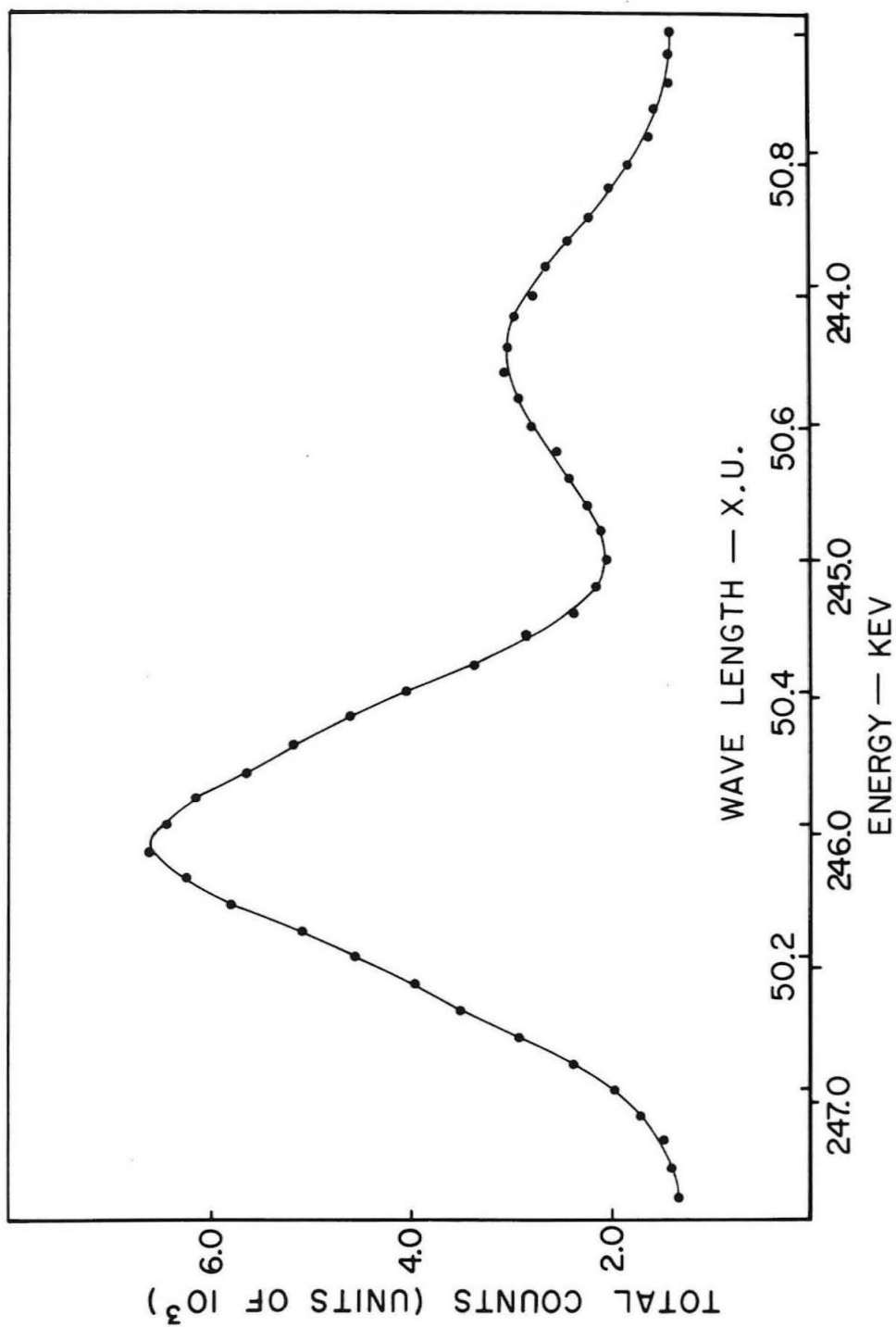


Fig. 6. The 246.056 and 244.264 kev gamma-ray lines in W<sup>183</sup> observed with the quartz (310) plane.

PART TWO

NUCLEAR-RESONANCE EXCITATION IN  $F^{19}$  AND  $Mn^{55}$

## I. INTRODUCTION

In this part of the thesis we will present the results of measurements of the resonance energy and width of the first excited levels of  $F^{19}$  and  $Mn^{55}$ . The experiment was performed by observing the scattered radiation from nuclei exposed to nearly mono-energetic x-rays selected from the bremsstrahlung spectrum of an x-ray tube by the bent-crystal monochromator described in Part One. It has long seemed desirable to use this technique; however, previous to the research reported here no successful measurement of nuclear-resonance excitation using this method has been reported.

Experimenters have used a variety of different techniques to excite low-lying nuclear states from their respective ground states. The techniques which have been most useful in the energy region below a few Mev can be placed into four groups: (i) "Coulomb-excitation" reactions in which the nuclear excitation results from interaction of the nucleus with the electromagnetic fields of bombarding particles, (ii) resonance excitation by means of gamma radiation emitted by a radioactive source, (iii) techniques which use a nuclear reaction to provide a Doppler shifted source of gamma radiation for nuclear excitation, and (iv) techniques using a portion of the continuous bremsstrahlung radiation.

The different experimental techniques for nuclear-resonance excitation mentioned above have a great deal in common in the methods of measurement and in the analysis of the experimental results obtained. The experimental techniques both supplement and check each other

regarding the information they supply about the properties of the nucleus. Below we summarize the experimental techniques which have been used for observing nuclear excitation according to methods (i) through (iv) and the results which can be obtained from the measurements.

As discussed in a review article by Alder, Bohr, Huus, Mottelson, and Winther (12) one can determine from Coulomb-excitation yield measurements the nuclear-transition energies, transition probabilities, and to some extent the multipole order of the transitions. The Coulomb-excitation technique has been especially fruitful in the determination of the electric-quadrupole transition-probability  $B(E2)$ . Measurements of the energy distribution and angular distribution of the decay radiation have given information about the nuclear decay scheme including the spins and energies of the resonance levels and the multipolarities and mixing ratios of the transitions observed.

Several successful experimental techniques which use a radioactive source to supply the excitation have been developed recently. The main goal of these resonance-excitation studies has been the determination of transition probability of the nuclear energy levels. The experimental procedure is to use gamma rays emitted from radioactive nuclei in transitions to their ground states to supply radiation in the narrow energy region of the absorption line in identical target nuclei. Early experiments using the radioactive source technique were not successful because the recoil energy loss to the nucleus in the emission and absorption process is large compared to the energy width of the nuclear level. As a result the cross

section for the interaction between the radiation and the target nuclei is very small. Once this problem was recognized several methods for restoring the resonance condition by the creation of special source and absorber conditions were found.

Metzger (13) reviews some of the basic formulas used in the analysis of resonance-excitation experiments and describes the following methods through which nuclear excitation has been observed using a radioactive source: (i) Moon and Storruste (14) have observed nuclear excitation by an ultra-centrifuge technique. They attach the source to the periphery of an ultra-centrifuge and use the gamma rays emitted tangentially in the direction of the motion. The increase in the energy of the radiation due to the Doppler shift caused by the motion of source nuclei with respect to the laboratory is sufficient to compensate for the recoil energy loss and restore the resonance condition. (ii) Malmfors (15) and later Metzger (16) have used the line broadening caused by the thermal motion of the emitting and absorbing nuclei to observe a nuclear-excitation effect. In the free recoil approximation the half-widths of the emission and absorption lines are proportional respectively to the square root of the source temperature and the absorber temperature. In certain cases the increase in the overlap between the emission and absorption lines by heating the source and (or) the absorber is sufficient to result in an observable resonance effect. (iii) Resonance-excitation experiments which use the Doppler-shifted gamma-rays emitted from

source nuclei which are in motion as a result of a preceding nuclear gamma decay or beta decay have been described by Metzger.

A special type of nuclear-excitation measurement with a radioactive source by the method of recoilless resonance absorption has recently been discovered by Moessbauer (17, 18). Moessbauer found that for a fraction of events, gamma emission and absorption take place with no change in the energy state of the crystal lattice. For these transitions the recoil momentum is absorbed by the crystal as a whole and the recoil energy loss is negligibly small. As a result the resonance condition is satisfied, and by suitable experimental arrangements sharp absorption lines approximately twice the natural nuclear-resonance width can be observed.

Nuclear reactions on light nuclei have been used by several experimenters (19, 20) as a source of gamma radiation for nuclear-resonance excitation. In these experiments resonance excitation is observed using the Doppler-shifted gamma-rays emitted by recoiling excited nuclei formed as a result of a nuclear reaction. The technique is best suited for the measurement of nuclear lifetimes which are short compared to the time between consecutive collisions of the recoiling nuclei with the surrounding material.

The possibility of observing nuclear-resonance excitation using continuous radiation from a betatron was first discussed by Schiff (21). A review of some experiments using betatron bremsstrahlung for nuclear excitation at energies greater than 5 Mev is given by Devons (22). Some more recent work on resonance scattering of bremsstrahlung in the region from 3 to 20 Mev from a linear accelerator is described

by Seward (23). Booth (24) has successfully used bremsstrahlung from an electron Van de Graaff for nuclear excitation in the energy region from 0.5 to 2.5 Mev.

The method of nuclear excitation with a diffracted x-ray beam has not been successfully used previous to the research in this thesis. With this method one is not restricted by special absorber conditions or by recoil problems occurring in resonance-excitation experiments with a radioactive source. The use of crystal diffraction to select a narrow band of x-rays from the bremsstrahlung spectrum results in a considerable reduction in problems due to the background from non-resonance radiation present in experiments in which the entire bremsstrahlung spectrum is incident on the scattering sample. The information on nuclear properties which can be obtained is in many ways similar to the information obtained through Coulomb-excitation experiments. In addition to the excitation through the electric transitions one can study excitation of nuclei through magnetic multipole transitions. From the yields of the magnetic dipole excitation, for example, one can directly determine the magnetic transition probability  $B(M1)$ . Also, from angular correlation measurements in an external magnetic field at the target nucleus one can obtain the magnetic moments of excited states.

The advantage of the diffracted x-ray beam technique is obvious. However, the energy resolution which can presently be obtained from x-ray diffraction is several orders of magnitude larger than the energy width of nuclear-resonance absorption-lines. As a result the nuclear-excitation effect has to be observed in the presence of a large

background from non-resonant electronic scattering. The main problems in the experimental technique are therefore: (i) that of obtaining sufficient x-ray intensity in the narrow region of the absorption line and (ii) that of reducing the non-resonant background effects to a minimum. In Chapter II cross-section formulas for the various interactions of photons with nuclei and atomic electrons are discussed. Chapter III contains a description of the experiment and the analysis of the data. Chapter IV gives a summary of the final results obtained and a comparison of these results with those of other experiments.

## II. INTERACTIONS OF ELECTROMAGNETIC RADIATION WITH MATTER

There are a number of processes through which photons can interact with matter. Following Fano (25) and Evans (26), interactions of electromagnetic radiation with matter can be classified in the following systematic form:

<u>Kinds of interaction</u>	<u>Effects of interaction</u>
I. Interaction with atomic electrons	A. Complete absorption
II. Interactions with nucleons	B. Elastic scattering
III. Interactions with electric field surrounding nuclei or electrons	C. Inelastic scattering
IV. Interaction with mesons field surrounding nucleons	

The twelve different ways of combining the two columns give the processes by which photons can be absorbed or scattered. In this experiment we observe the ratio of the cross section for nuclear-resonance scattering II B to the cross section for the Compton scattering I C. Cross sections for these interactions are discussed in detail below.

Also Rayleigh scattering from the atomic electrons I B is observed in the experiment as a background effect and is discussed in Appendix V. For completeness the names associated with some of the other interactions in the table are listed: photoelectric effect I A, Thomson scattering by nucleus II B, Delbruck scattering III B, pair production III A, photodisintegration of nuclei II A, and meson production IV A.

#### A. Cross Sections for Nuclear-Resonance Excitation

The dispersion theory cross section for nuclear-resonance photo-excitation followed by de-excitation through the  $b^{\text{th}}$  channel is (13, 27)

$$\sigma_{a,b} = \frac{\pi \lambda^2}{2} \cdot \frac{(2J_1 + 1)}{(2J_0 + 1)} \cdot \frac{\Gamma_a \Gamma_b}{(E - E_r)^2 + (\Gamma/2)^2} \quad (7)$$

where  $J_1$  and  $J_0$  are the total angular momentum of the excited state and the ground state, respectively,  $E_r$  is the resonance energy,  $E$  is the energy of the incident photon,  $\lambda$  is the corresponding wavelength divided by  $2\pi$ ,  $\Gamma_a$  is the partial width for the direct gamma-ray transition to the ground state,  $\Gamma_b$  is the partial width for de-excitation through the  $b^{\text{th}}$  decay channel, and  $\Gamma = \sum_i \Gamma_i$  is the natural width of the level. The factor of two in the denominator of Eq. 7 expresses the multiplicity caused by the two possible polarizations of the photons.

In our use of this equation the exit channel  $b$  corresponds to the entrance channel  $a$ . Therefore,

$$\Gamma_b = \Gamma_a. \quad (8)$$

We note that in this case the interaction described by Eq. 7 has the classification II B, elastic nuclear scattering. Small terms resulting from nuclear Thomson scattering have been neglected. When  $b$  does not correspond to the entrance channel the interaction described by Eq. 7 has the classification II C, inelastic nuclear scattering.

In our application it is convenient to rewrite Eq. 7. When the effect of internal conversion is included the natural width of the first excited level is

$$\Gamma = \Gamma_a + \alpha \Gamma_a = (1 + \alpha) \Gamma_a \quad (9)$$

where  $\alpha$  is the conversion coefficient. Then Eq. 7 becomes

$$\sigma_{a,a} = \frac{\sigma_o (\Gamma/2)^2}{(E - E_r)^2 + (\Gamma/2)^2} \quad (10)$$

where

$$\sigma_o = \frac{2\pi \lambda^2}{(1 + \alpha)^2} \cdot \frac{(2J_1 + 1)}{(2J_o + 1)} \quad (11)$$

### B. Crystal Binding and Doppler Effects

In analysis of nuclear-resonance excitation one must use cross-section formulas which take account of the dynamics of the atomic motion. Lamb (28) has treated this problem in connection with neutron resonance experiments, and his discussion also applies to the gamma-ray problem. Singwi and Sjolander (29) give an analysis in which they account for the dynamics of the atomic motion through a space-time self-correlation function. For our purposes the results they

obtain for the effective resonance-excitation cross sections are the same as those obtained from Lamb's analysis.

Through an application of the formalism of Singwi and Sjolander the cross section for resonance absorption of gamma rays by atoms in a crystal lattice can be evaluated. For the case of weak binding ( $2W \gg 1$ ) and using the Debye approximation the nuclear cross section is given by

$$\sigma_n(E) = \frac{\sigma_0 \Gamma^2}{4} \cdot \frac{\exp-2W}{(E - E_r)^2 + (\Gamma/2)^2} + \frac{\sigma_0 \Gamma}{2\pi^{1/2} \Delta} \int_{-\infty}^{+\infty} \frac{dz}{z^2 + 1} \exp\left[-(\Gamma/2\Delta)^2(x - z)^2\right] \quad (12)$$

$$x = 2(E - E_r - R)/\Gamma; \quad R = E_r^2/2Mc^2 = \text{recoil energy}; \quad (13)$$

$$\Delta^2 = 4RkT \left[ \frac{3}{2} \left( \frac{T}{\Theta} \right)^3 \int_0^{\Theta/T} \frac{y^3(\exp y + 1)dy}{(\exp y - 1)} \right] \equiv 4RkT \beta(\Theta/T); \quad (14)$$

$$W = \frac{3R}{k\Theta} \left[ \frac{1}{4} + \left( \frac{T}{\Theta} \right)^2 \int_0^{\Theta/T} \frac{ydy}{(\exp y - 1)} \right] \equiv \frac{3R}{k\Theta} \left[ \frac{1}{4} + \frac{T}{\Theta} \chi(\Theta/T) \right] \quad (15)$$

where  $T$  is the crystal temperature,  $\Theta$  is the crystal Debye temperature,  $Mc^2$  is the rest energy of the nucleus, and  $k$  is the Boltzmann's constant. Numerical values for the function  $\beta(x)$  and  $\chi(x)$  are given in Table IV. Tables of values for integral in Eq. 12 are given by Rose, Miranker, Leak, Rosenthal, and Henrickson (30).

The first term in Eq. 12 is the sharp resonance cross section for recoilless absorption and agrees with the formulas given by

TABLE IV. Tabulation of Values for  $\chi(x)$  and  $\beta(x)$

$x$	$\chi(x)$	$\beta(x)$
1.0	0.777	1.05
2.0	0.607	1.19
3.0	0.480	1.41
4.0	0.388	1.68
5.0	0.321	1.99
6.0	0.271	2.33
7.0	0.234	2.68
8.0	0.205	3.04

Moessbauer (17) and Lipkin (31). The second term in Eq. 12 can be compared with the usual effective absorption cross section which is obtained when one considers resonance excitation of nuclei in a perfect gas (13). In this comparison the results are found to be identical except for the value assigned to the Doppler width  $\Delta$ . For the perfect gas case the Doppler width is

$$\Delta_p^2 = 4RkT. \quad (16)$$

In the limit of high temperature the value for  $\Delta$  given by Eq. 14 approaches the value of  $\Delta_p$ .

Finally we obtain the resonance-absorption cross-section formula used in Chapter III for analysis of the experiment. The effect of first term of Eq. 12 is negligibly small compared to that of the second term; therefore, we neglect it. Also we approximate the second term using the fact that  $\Delta \gg \Gamma$  and  $R \ll E_r$ . Then, as is shown by Metzger (13), the effective resonance excitation cross section is given by

$$\sigma_n(E) = \frac{\sigma_0 \Gamma \pi^{1/2}}{2\Delta} \exp\left[-(E - E_r)/\Delta\right]^2. \quad (17)$$

We will also be interested in the integral of  $\sigma_n(E)$  over energy. Extending the integration from  $-\infty$  to  $+\infty$

$$\int_{-\infty}^{+\infty} \sigma_n(E) dE = \sigma_0 \Gamma \pi^{1/2}. \quad (18)$$

This result is true for any  $\Delta / \Gamma$  (13).

### C. Cross Section for Compton Scattering

The Compton scattering process is described in a number of places, e.g., Evans (26). Heitler (32). For later reference we give

here a summary of some of the formulas related to this process. The formulas are for the case of incident photon being scattered by an electron which is assumed to be unbound and initially at rest.

The equation for the energy of the scattered photon is obtained from the laws of conservation of energy and momentum. The equation is (26)

$$E' = E / \left[ 1 + \alpha_0 (1 - \cos \xi) \right]; \quad \alpha_0 = E/mc^2 \quad (19)$$

where E and E' are the energies of the incident and scattered photons, respectively,  $mc^2$  is the rest energy of an electron, and  $\xi$  is the scattering angle.

The differential collision cross section per unit solid angle for incident unpolarized radiation is given by (26)

$$\frac{d\sigma_c}{d\Omega} = \frac{r_0^2}{2} \left[ \frac{1 + \cos^2 \xi}{1 + \alpha_0 (1 - \cos \xi)} \right]^2 \left[ 1 + \frac{\alpha_0^2 (1 - \cos \xi)^2}{(1 + \cos^2 \xi)(1 + \alpha_0 (1 - \cos \xi))} \right] \quad (20)$$

where  $r_0$  is the classical electron radius. Replacing  $d\Omega$  in Eq. 20 by  $2\pi \sin \xi d\xi$  and integrating over all possible  $\xi$  gives the total collision cross section (26)

$$\begin{aligned} \sigma_c(E) = \int_0^\pi d\sigma_c = 2\pi r_0^2 & \left[ \frac{1 + \alpha_0}{\alpha_0^2} \left( \frac{2(1 + \alpha_0)}{1 + 2\alpha_0} - \frac{1}{\alpha_0} \ln(1 + 2\alpha_0) \right) \right. \\ & \left. + \frac{1}{2\alpha_0} \ln(1 + 2\alpha_0) - \frac{1 + 3\alpha_0}{(1 + 2\alpha_0)^2} \right] \quad (21) \end{aligned}$$

Grodstein (33) discusses the effect of electron binding on the Compton cross section for atoms. For our purposes the atomic Compton cross section is given by the product of the atomic number and  $\sigma_c$  given by Eq. 21.

### III. DESCRIPTION OF THE EXPERIMENT

The monochromator described in Part One of this thesis was used to supply a beam of monoenergetic x-rays. Figure 7 shows the arrangement for the experiment. A bent-germanium (or quartz) crystal is used to diffract a nearly monoenergetic beam of x-rays from the bremsstrahlung spectrum of the x-ray source (anode of an x-ray tube). The diffracted beam passes through the collimator and is incident on the scattering sample. Radiation scattered through an angle of about 135 degrees is observed with a NaI scintillation detector. The scattering sample is mounted in a vacuum scattering chamber, and the radiation shielding is arranged so that the detector observes scattering from the sample only. Pulses from the detector are amplified by a standard "Hamner model No. 300" amplifier. Two "Hamner model No. N 302" pulse-height analyzers are connected to the amplifier output. One of these is set to select pulses from the detector whose height corresponds to that of elastically scattered photons. The second pulse-height analyzer is set to select pulses whose height corresponds to that of inelastically Compton-scattered photons. Also a "Penco" 100-channel pulse-height analyzer is periodically used during the experiment to observe the entire pulse spectrum from the scintillation detector.

With this experimental equipment several different measurements of the scattered radiation from scattering samples of lithium fluoride and manganese were made. Essentially, the experimental observations give the ratio of the number of elastically-scattered photons to the

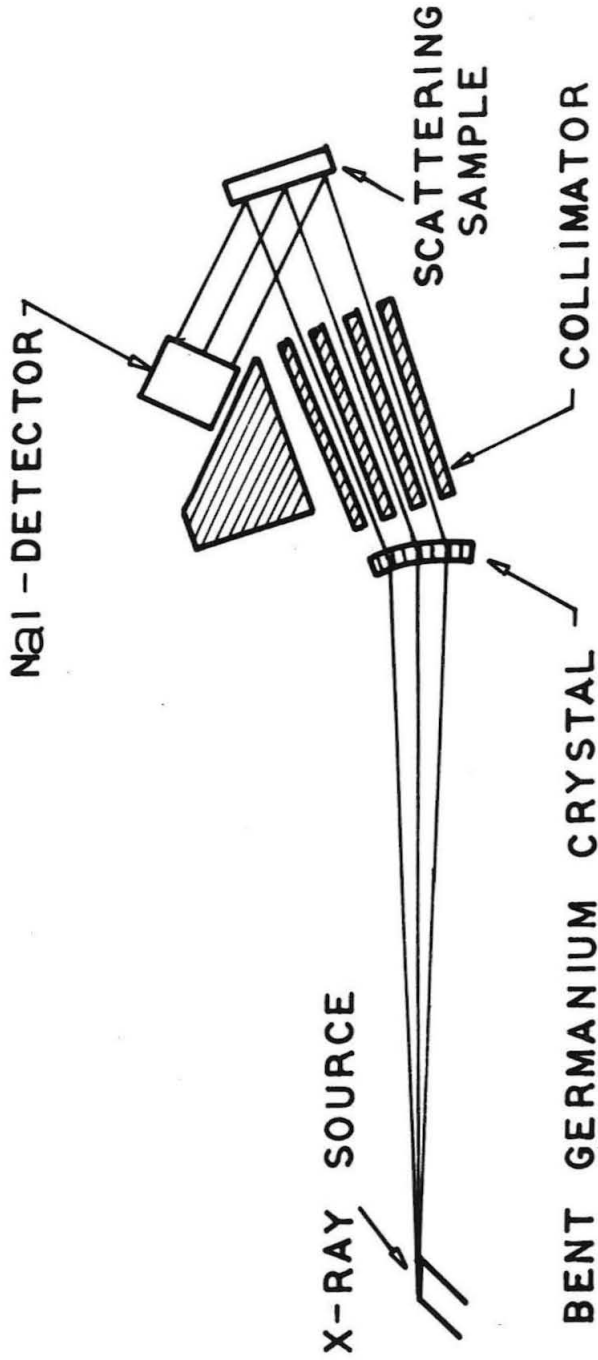


Fig. 7. Schematic arrangement for the nuclear-resonance excitation-experiment. The bent-germanium crystal is used to diffract a nearly monoenergetic beam of x-rays from the bremsstrahlung spectrum of the x-ray source (anode of an x-ray tube). The diffracted beam passes through the collimator and is incident on the scattering sample. The radiation scattered through 135° is observed with a NaI detector.

number of inelastically Compton scattered photons as a function of the wavelength of the incident x-ray beam. A nuclear-resonance excitation-peak is observed at the wavelength corresponding to the energy of the nuclear level; therefore, the wavelength position of the peak gives directly the energy position  $E_r$  of the level. The energy width  $\Gamma$  of the level is determined from the observed yield through a formula which is derived in Section A. The experimental observations and results are presented in Section B.

#### A. Formula for the Experimental Determination of the Resonance Width

In this section we obtain the formula used in the analysis of the experimental data to obtain the width  $\Gamma$  of the nuclear resonance observed. We assume that no multiple scattering of photons occur in the scatterer, that the detector efficiency is independent of photon energy, and that the Compton and nuclear scattering is isotropic. In the analysis of the data with the formula to be derived here, corrections resulting from the neglect of these effects are required and are discussed in Appendix III. We consider here the case of a thin scattering sample. The case of a sample of arbitrary thickness is discussed in Appendix II.

For a thin scattering sample  $NL\sigma(E_r) \ll 1$  where  $N$  is the atomic density,  $L$  is the sample thickness, and  $\sigma(E_r)$  is the total cross section at the resonance energy for interaction of photons with the atoms of the scatterer. The counting rate  $R'_n(E_m)$  due to nuclear scattering in the sample is given by

$$R'_n(E_m) = CNL \int_0^\infty \sigma_n(E) \phi(E - E_m) dE \quad (22)$$

where  $\sigma_n(E)$  is the nuclear-scattering cross section given by Eq. 17,

$\phi(E-E_m)$  is the flux of photons incident on the scattering sample with energy between  $E$  and  $E+dE$  when the monochromator is set at the energy  $E_m$ , and  $C$  is a constant which is determined by the solid angle and the efficiency of the detector. The lower limit of integration can be changed from 0 to  $-\infty$  with no significant change in the result. With no further mention we will do this in all the following formulas. In the experiment  $\phi(E-E_m)$  is approximately given by a Gaussian with an energy width several orders of magnitude larger than the Doppler width of the nuclear resonance. Therefore we can replace  $\phi(E-E_m)$  by  $\phi(E_r-E_m)$  in Eq. 22 and obtain

$$R'_n(E_m) = CNL \phi(E_r - E_m) \int_{-\infty}^{+\infty} \sigma_n(E) dE. \quad (23)$$

Substitution of Eq. 18 gives

$$R'_n(E_m) = \frac{\pi CNL \sigma_0 \Gamma}{2} \phi(E_r - E_m). \quad (24)$$

The counting rate  $R'_c(E_m)$  from Compton scattering is given by

$$R'_c(E_m) = CNLZ \int_{-\infty}^{+\infty} \sigma_c(E) \phi(E - E_m) dE \quad (25)$$

where  $\sigma_c(E)$  is the Compton scattering cross section given by Eq. 21,  $C$  is the solid angle and efficiency factor, and  $Z$  is the atomic number of the scattering atoms. Since  $\sigma_c(E)$  is slowly varying in  $E$  compared to  $\phi(E-E_m)$ , we replace  $\sigma_c(E)$  by  $\sigma_c(E_m)$  in Eq. 25 and obtain

$$R'_c(E_m) = CNLZ \sigma_c(E_m) \int_{-\infty}^{+\infty} \phi(E - E_m) dE. \quad (26)$$

Taking the ratio of Eqs. 24 and 26 at  $E_m = E_r$  and solving for  $\Gamma$  gives.

-40-

$$\Gamma = \frac{2Z \sigma_c(E_r)}{\pi \sigma_0} \cdot \frac{R_n'(E_r)}{R_c'(E_r)} \cdot \frac{\int_{-\infty}^{+\infty} \phi(E - E_r) dE}{\phi(0)} \quad (27)$$

Further we note that from Eq. 23

$$\phi(E - E_r) \propto R_n'(E) \quad (28)$$

Therefore Eq. 27 becomes

$$\Gamma = \frac{2Z \sigma_c(E_r)}{\pi \sigma_0} \cdot \frac{\int_{-\infty}^{+\infty} R_n'(E) dE}{R_c'(E_r)} \quad (29)$$

Assuming that  $\sigma_c(E_r)$  is known and that the information required to calculate  $\sigma_0$  from Eq. 11 is known, Eq. 29 gives the nuclear-resonance width in terms of the experimentally observed quantities  $R_n'(E)$  and  $R_c'(E)$ .

In Appendix II a formula similar to Eq. 29 is derived for a scattering sample of arbitrary thickness. The formula obtained can be written

$$\frac{\delta \int_{-\infty}^{+\infty} R_n(E) dE}{R_c(E_r)} = A(\Gamma) \quad (30)$$

where  $A(\Gamma)$  is given by Eq. 56,  $R_n(E)$  and  $R_c(E)$  are the counting rates observed due to nuclear and Compton scattering in the scattering sample, and  $\delta$  is a correction factor which is discussed in Appendix III. The correction factor  $\delta$  is introduced into the equation to account for the effects of multiple scattering of photons in the sample, variation of detector efficiency with incident photon energy and anisotropy in the Compton and nuclear scattering. Eq. 30 is an implicit equation from which the nuclear-resonance width can be determined from the observed experimental results.

We now obtain the form of Eq. 30 which is used for the analysis of the experimental data. It is convenient to assume a Gaussian

distribution\* in wavelength for the incident flux. Then according to Eq. 28 (or for the thick sample case Eq. 52) we can write

$$R_n(E_m) = R_n(E_r) \exp - 2.773 \left[ (\lambda_m - \lambda_r) / \tau \right]^2 \quad (31)$$

where  $\tau$  is the full-width at one-half maximum.

Multiplying by  $dE$  and integrating gives

$$\int_{-\infty}^{+\infty} R_n(E) dE = R_n(E_r) \int_{-\infty}^{+\infty} \frac{d\lambda}{\lambda} E \exp - 2.773 \left[ (\lambda - \lambda_r) / \tau \right]^2 \quad (32a)$$

$$= 1.065 \frac{E_r \tau}{\lambda_r} R_n(E_r) \quad (32b)$$

where we have replaced  $E/\lambda$  by  $E_r/\lambda_r$  in the integration. Inserting this result into 30 gives

$$\frac{\int R_n(E_r) \tau}{R_c(E_r)} = 1.065 \frac{\lambda_r}{E_r} A(\Gamma) \equiv B(\Gamma) \quad (33)$$

This equation is used in the following sections for the determination of the nuclear-resonance width from the observed experimental results. The nuclear width  $\Gamma$  is determined by comparing the experimental value obtained for the left side of Eq. 33 with the tabulation of the right side given for various values of  $\Gamma$  in Tables V and VI of Appendix II.

\* Several authors, DuMond (3), Lind (34), and Edwards (11), have discussed factors which contribute to window profile for a curved crystal monochromator. The correct distribution function consists of a fold of functions describing the crystal reflectivity, the source spacial distribution, the source spectral profile, and imperfections in the focus of the bent crystal. The assumption of a Gaussian distribution made in the analysis of the data in this experiment has been justified to the accuracy of the results obtained.

## B. Results of the Experiments With a Lithium Fluoride Scattering Sample

For the study of the first-excited level in  $F^{19}$  a scattering sample was prepared using powdered lithium fluoride. The physical dimensions of the sample were 8.0 x 8.0 x 1.9 cm. Two sheets of 0.0025 cm thick mylar bound the lithium fluoride powder and form the window through which the electromagnetic radiation passes. Their contribution to the total scattering and absorption is completely negligible. By weighing the sample during the construction, the thickness of the lithium fluoride was determined to be 1.32 gm/cm<sup>2</sup>.

With this sample, three experiments were performed in which nuclear-resonance excitation of the first-excited level of  $F^{19}$  was observed.

1. In the first experiment performed with the lithium fluoride scattering sample, a quartz crystal in first-order diffraction from the (310) planes was used in the monochromator, and the nuclear-excitation peak was observed on both sides of the monochromator zero position. Figure 8 shows a typical pulse-height spectrum observed from the NaI detector during the experiment. As indicated by the arrow on the figure, this pulse spectrum was observed at an incident photon energy of 109.887 kev. The large peak at 81.0 kev results from the photons which are Compton scattered by the electrons in the sample. The elastic peak from the nuclear-resonant scattered photons which occurs at 109.887 kev is too small to be seen on the figure. This elastic peak has been observed by comparing pulse

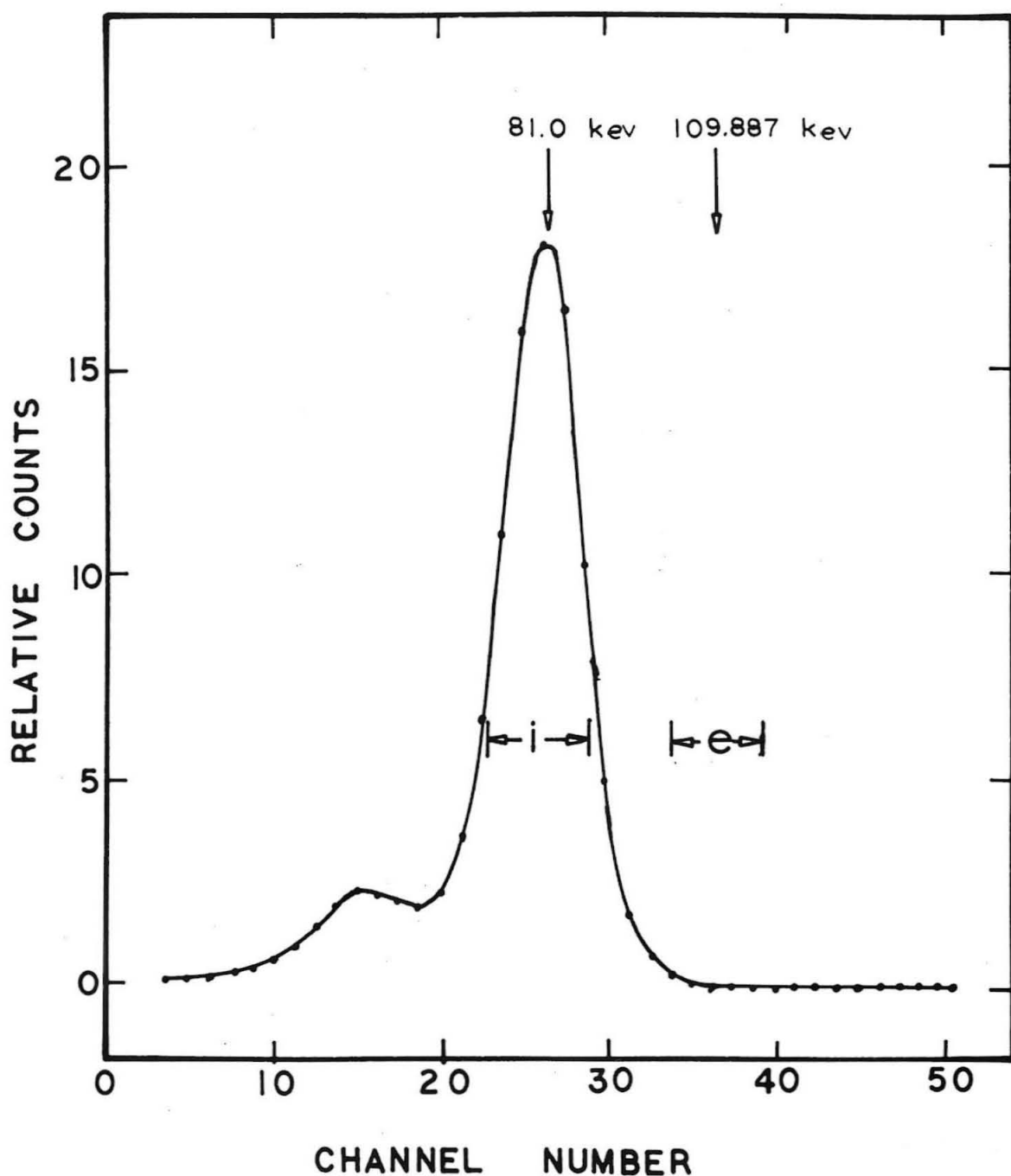


Fig. 8. Pulse spectrum observed from NaI detector resulting from scattering of 109.887 keV incident photons by a lithium fluoride sample. The regions "e" and "i" correspond to the pulse height settings for the two single channel analyzers used to observe respectively the elastically and inelastically scattered radiation.

spectra with monochromator settings on and off the resonance position and will be discussed on page 47. In this experiment the two pulse-height analyzers mentioned on page 36 were set to observe, respectively, elastically and inelastically scattered radiation. The analyzer settings are indicated by "e" and "i" on the figure. We will denote the counting rates observed at a monochromator setting  $\lambda_m$  as  $R_e(\lambda_m)$  for the elastic channel and  $R_i(\lambda_m)$  for the inelastic channel.

Figure 9 shows a resonance peak resulting from resonance excitation of the first-excited level in  $F^{19}$ . The ordinate of the figure is the observed ratio  $R_e(\lambda_m)/R_i(\lambda_m)$ , and the abscissa is the monochromator wavelength setting  $\lambda_m$ . The data shown in the figure were accumulated in the following manner. With automatic recording equipment the monochromator was caused to record counts from the pulse-height analyzers for two minutes sequentially at each of ten monochromator wavelength positions spaced at intervals of 0.08 x-units over the resonance position. At the completion of this 20 minute cycle the monochromator automatically returned to the starting position and repeated the cycle. A data run consisted of data accumulated on one side of the monochromator zero wavelength position for 63 cycles. The points shown on Fig. 9 represent the average of four data runs taken alternately on one side (positive side) then on the other side (negative side) of the monochromator zero wavelength position. Periodically during each data run the  $W_k$  x-ray calibration line from the  $\alpha_1$

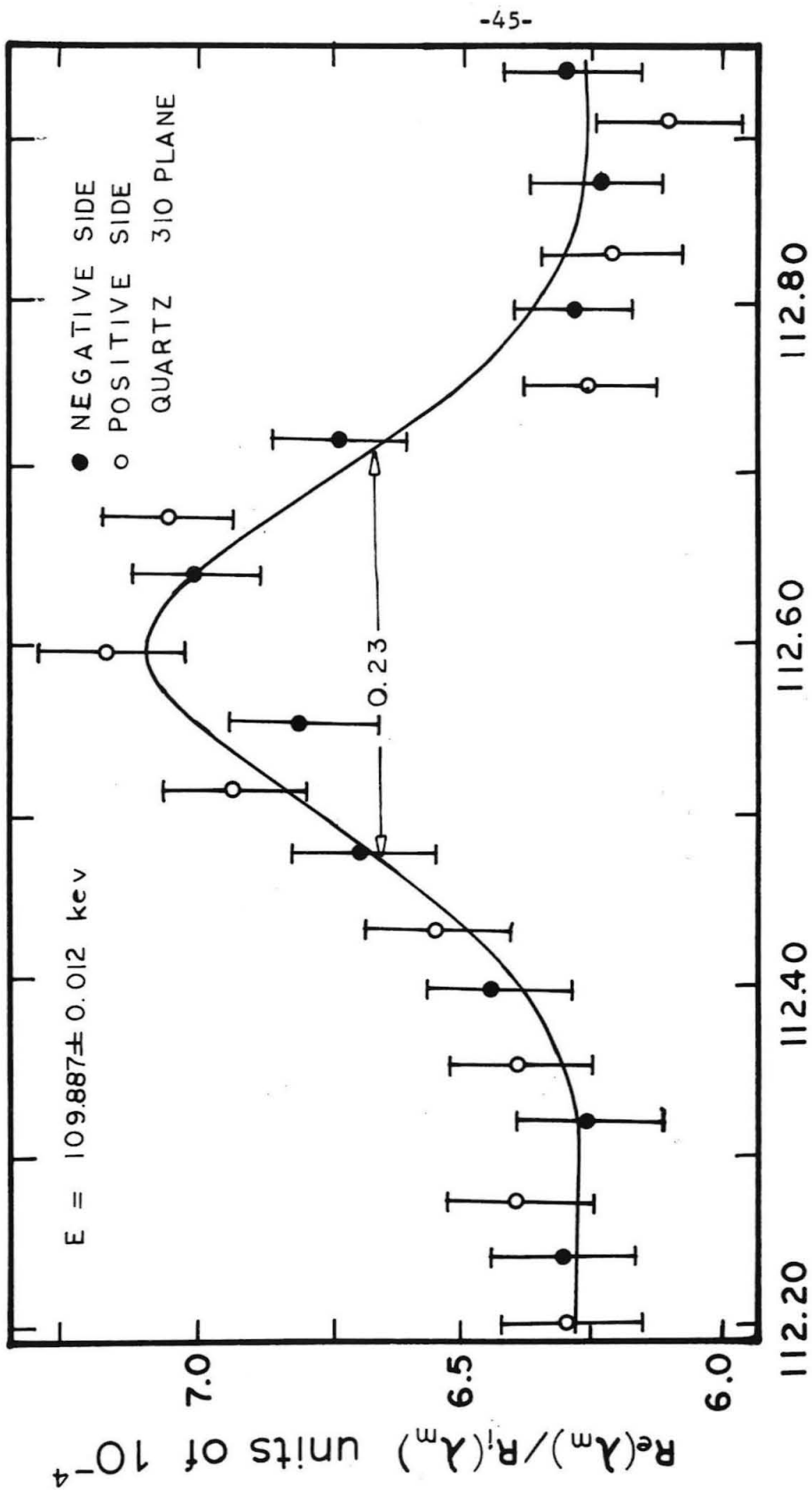


Fig. 9. Nuclear-resonance excitation of the first-excited state in  $F^{19}$  observed with a quartz diffraction crystal. The figure shows the ratio of elastic to inelastic scattered radiation from a lithium fluoride sample as a function of the wavelength of the incident beam.

tungsten x-ray tube was measured to obtain a check on the monochromator zero position. The wavelength settings of the monochromator shown on Fig. 9 were determined relative to 208.571 x-units for the  $W_{K\alpha_1}$  x-ray calibration line.

Some typical counting rates observed in the experiment are given in the following table:

	Monochromator Wavelength Position	
	112.590 x-units	112.190 x-units
$R_e(\lambda_m)$	$8.88 \pm 0.17 \frac{\text{counts}}{\text{minute}}$	$7.74 \pm 0.18 \frac{\text{counts}}{\text{minute}}$
$R_i(\lambda_m)$	12,340 "	12,375 "

The curve drawn through the data in Fig. 9 is given by the equation

$$\frac{R_e(\lambda_m)}{R_i(\lambda_m)} = a_1 + a_2 \exp-2.773 \left[ (\lambda_m - \lambda_r) / \tau \right]^2 \quad (34)$$

where  $\lambda_m$  is the monochromator setting and

$$\begin{aligned} a_1 &= (6.26 \pm 0.06) 10^{-4}, & a_2 &= (8.5 \pm 1.2) 10^{-5}, \\ \tau &= 0.23 \pm 0.04 \text{ x-units}, & \lambda_r &= 112.592 \pm 0.012 \text{ x-units}. \end{aligned} \quad (35)$$

The parameters  $a_1$ ,  $a_2$ ,  $\tau$ , and  $\lambda_r$  were determined by a least-square fit of the formula to the data points. The use of this equation for fitting data is justified in Appendix IV.

From the value of  $\lambda_r$  we deduce directly the resonance energy

$$E_r = 109.887 \pm 0.012 \text{ kev.} \quad (36)$$

The nuclear-resonance width is determined from the values of  $a_2$  and  $\tau$ . It is shown in Appendix IV that

$$\frac{R_n(E_r)}{R_c(E_r)} = a_2 \cdot \frac{\epsilon_i}{\epsilon_e} \left[ \frac{R_i(\lambda_r)}{R_i(\lambda_r) - R_i^{bgd}(\lambda_r)} \right] \quad (37)$$

where  $\epsilon_e$  and  $\epsilon_i$  are efficiency factors which result from the finite width of the single-channel pulse-height analyzers and  $R_i^{bgd}(\lambda_r)$  is the counting rate observed in the inelastic counting channel when the diffracted beam is not incident on the scattering sample. As is discussed in Appendix IV the efficiency factors and the quantity in the brackets in Eq. 37 were determined from experimental data obtained preceding and following the collection of data for the points in Fig. 9.

From Eq. 37 the value  $(11.1 \pm 1.6)10^{-5}$  was determined for the ratio  $R_n(E_r)/R_c(E_r)$ . When the correction factor  $\delta$  obtained in Appendix III is included we obtain

$$\frac{\delta R_n(E_r)}{R_c(E_r)} = (11.6 \pm 1.6)10^{-5}. \quad (38)$$

The nuclear resonance width is determined by comparing the left side of Eq. 33, given by the experiment through Eq. 38 and the value of  $\tau$  in Eq. 35, with the tabulated values of  $B(\Gamma)$  given in Appendix II, Table V. From this comparison

$$\Gamma = (5.1 \pm 1.2)10^{-7} \text{ ev.} \quad (39)$$

2. In the second experiment performed with the lithium fluoride scattering sample, the resonance-excitation peak was observed in the pulse spectrum from the detector. In this experiment the

detector-pulse-height spectrum obtained using the "Penco" 100-channel analyzer was observed for monochromator wavelength settings

$\lambda_m = 112.092$  x-units,  $\lambda_m = \lambda_r = 112.592$  x-units, and  $\lambda_m = 113.092$  x-units. In the data accumulation five minute observations were taken alternately on and off the resonance for a total of 40 hours at each position. The pulse spectrum  $H(\text{channel number})$  obtained from the sum of the data observed at  $\lambda_m = \lambda_r$  is shown in Fig. 10 by the curve labeled  $H(N)$ . Also illustrated in Fig. 10 is the background pulse-spectrum  $G(\text{channel number})$  obtained from the sum of the spectra observed in the two off-resonance positions. The nuclear-excitation peak is seen in the difference  $H(N) - G(N)$  between these two spectra. The size of the excitation peak is more clearly illustrated in Fig. 11. Curve A of this figure is the ratio  $[H(N) - G(N)] / H(N)$ . Curve B gives the values observed for  $H(N) - G(N)$  in the region of the elastic peak. Curve C indicates the pulse-height distribution obtained for the 122.05 keV gamma ray from a  $\text{Co}^{57}$  source. The line shape and center position for the curve B was determined from that of the 122.05 keV calibration line.

The ratio of the integrated area under curve B of Fig. 11 to the area under the curve in Fig. 10 with a small background correction gives the value  $(7.9 \pm 1.9)10^{-5}$  for the ratio  $R_n(E_r)/R_c(E_r)$ . Multiplying by the correction factor  $\delta$  from Appendix III we obtain

$$\frac{\delta R_n(E_r)}{R_c(E_r)} = (8.3 \pm 2.0)10^{-5} \quad (40)$$

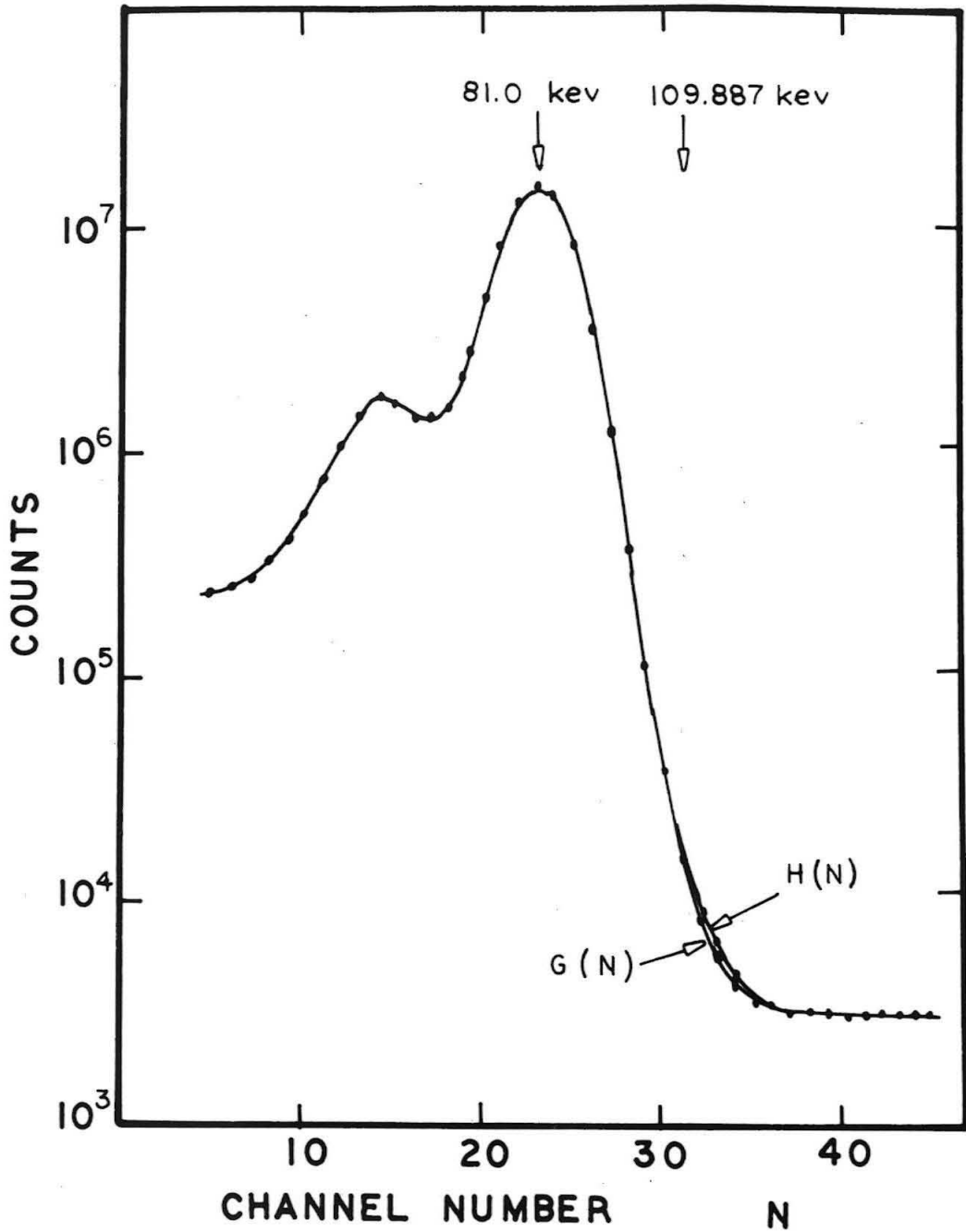


Fig. 10. Pulse spectra observed from the NaI detector resulting from photons scattered by the lithium fluoride sample. Curve H(N) is the spectrum observed with the monochromator set at the resonant position (112.592 x-units). Curve G(N) is the sum of pulse spectra obtained with the monochromator set at 112.092 x-units and 113.092 x-units.

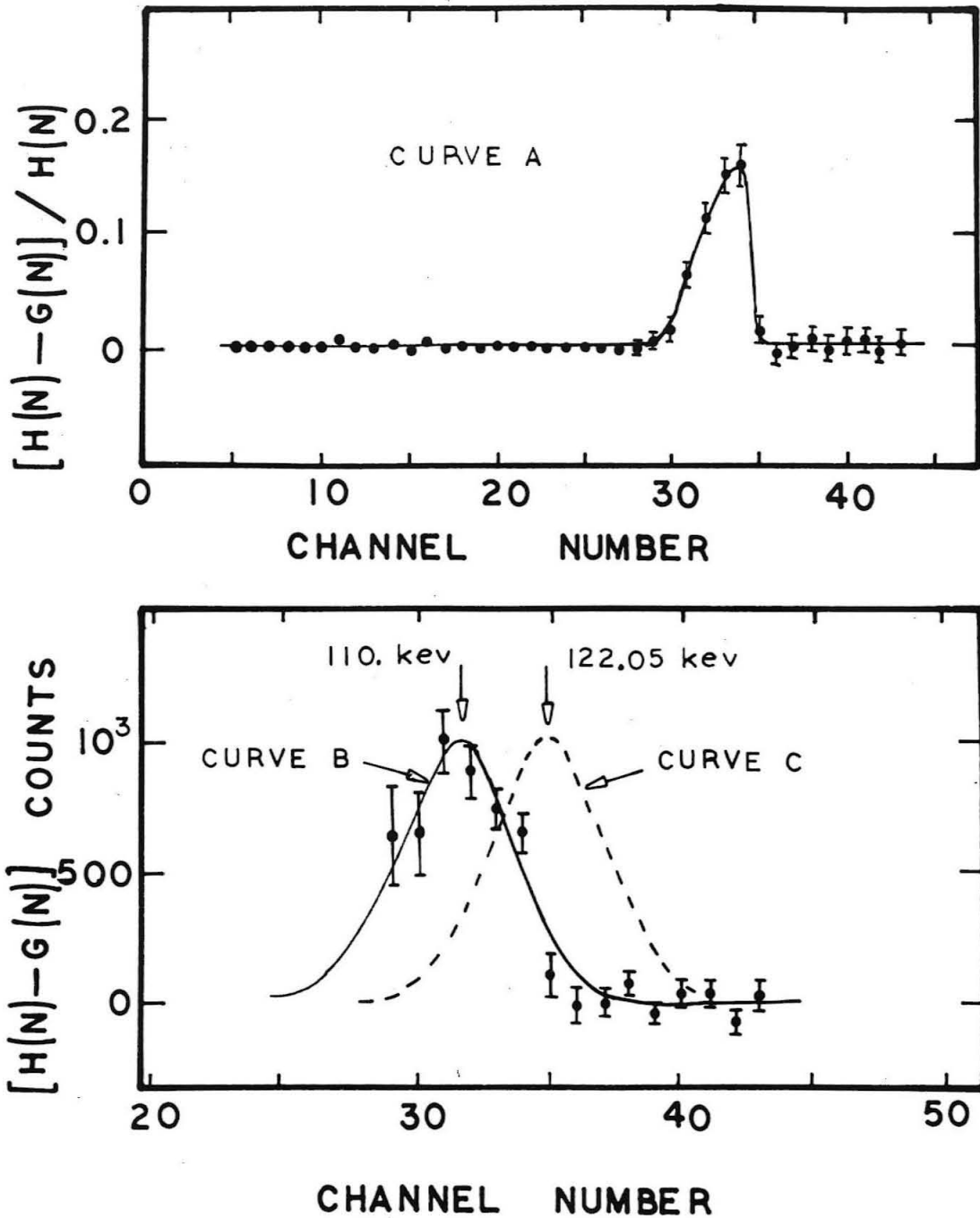


Fig. 11. Nuclear-excitation peak corresponding 109.887 keV photons observed in the pulse spectrum  $H(N)$  shown in Fig. 10. Curve A shows the relative effect observed. Curve B is the actual difference observed in the spectra. Curve C is a calibration curve obtained by using 122.05 keV gamma-rays from a  $Co^{57}$  source.

which is in agreement with the result given in Eq. 38 for experiment one.

Now using the result for  $\tau$  from experiment one we obtain the nuclear resonance width from Eq. 33

$$\Gamma = (3.7 \pm 1.2)10^{-7} \text{ ev.} \quad (41)$$

3. The procedure in a final measurement of nuclear excitation in  $F^{19}$  was identical to experiment one except that (i) a germanium-crystal (800) plane diffraction was used in the monochromator and (ii) the data was observed on only one side of the monochromator zero. Fig. 12 shows the results which were obtained. The wavelength settings of the monochromator were determined relative to 208.571 x-units for the  $W_{K\alpha_1}$  x-ray calibration line. Some typical counting rates observed in the experiment are given in the following table:

	Monochromator Wavelength Position	
	112.584 x-units	112.342 x-units
$R_e(\lambda_m)$	$13.66 \pm 0.19 \frac{\text{counts}}{\text{minute}}$	$12.24 \pm 0.19 \frac{\text{counts}}{\text{minute}}$
$R_i(\lambda_m)$	10,096 "	10,118 "

A least-square fit of Eq. 34 to the data points gave the following values for the parameters:

$$\begin{aligned} a_1 &= (11.96 \pm 0.12)10^{-4}, & a_2 &= (16.2 \pm 1.8)10^{-5} \\ \tau &= 0.162 \pm 0.026 \text{ x-units}, & \lambda_r &= 112.582 \pm 0.005 \text{ x-units.} \end{aligned} \quad (42)$$

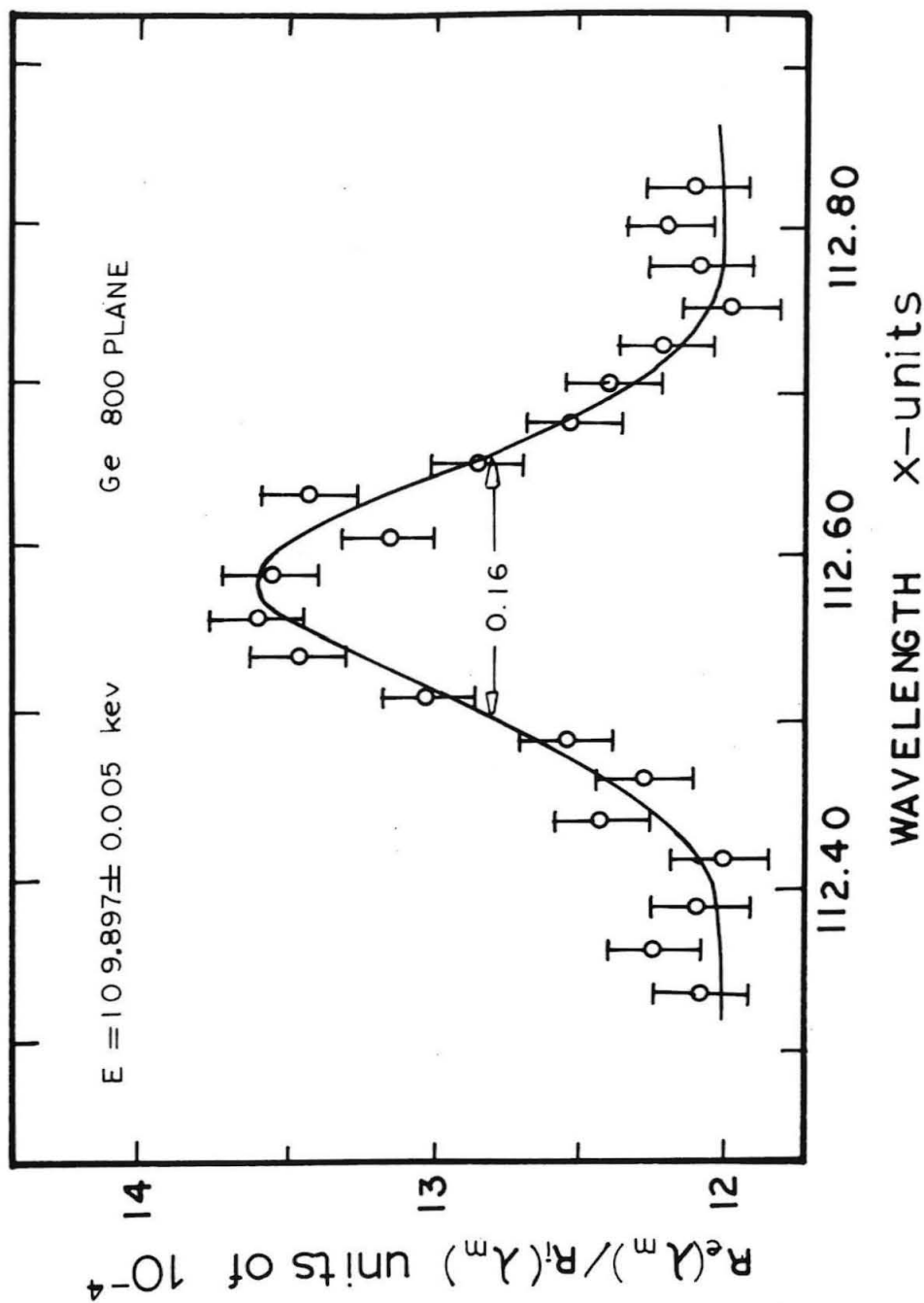


Fig. 12. Nuclear-resonance excitation of the first-excited state in  $F^{19}$  observed with a germanium-diffraction crystal in the monochromator. The figure shows the ratio of the elastic to the inelastic radiation from a lithium fluoride sample as a function of the wavelength of the incident beam.

The curve shown on Fig. 12 was calculated from Eq. 34 and the parameters given in Eq. 42

From the value of  $\lambda_r$  the resonance energy is

$$E_r = 109.897 \pm 0.005 \text{ kev.} \quad (43)$$

Proceeding as described for experiment one, the resonance width was determined to be

$$\Gamma = (6.5 \pm 1.2)10^{-7} \text{ ev.} \quad (44)$$

### C. Results of Experiments With a Manganese Scattering Sample

For the study of the first-excited level in  $Mn^{55}$  a scattering sample was prepared using powdered manganese. The physical dimensions of this sample are  $8.0 \times 8.0 \times 0.48$  cm. The thickness determined from the weight and area of the sample is  $3.21 \text{ gm/cm}^2$ .

The procedure for the experimental measurement of nuclear excitation in  $Mn^{55}$  is the same as the lithium fluoride experiment described on pages 42 to 47 except that (i) a germanium-crystal (800) plane diffraction was used in the monochromator and (ii) the data were observed on only one side of the monochromator zero. As in the previous experiments on lithium fluoride the tungsten  $W_{k\alpha_1}$  line from the x-ray tube was used to determine the monochromator wavelength setting.

Although the width of manganese resonance studied is actually larger than that of fluorine, the size of the relative nuclear-excitation effect observed in manganese is smaller. This results from an increase in the value for the observed ratio  $R_e(\lambda_m)/R_i(\lambda_m)$

caused by electronic Rayleigh scattering in the sample. This effect is discussed in Appendix V. Combining Eqs. 63 and 68 in the appendices the contribution of electronic scattering to the observed ratio  $R_e(\lambda_m)/R_i(\lambda_m)$  is seen to be  $(B_1 + B_2 Z^2 \lambda_m^3)/\epsilon_i$  where  $B_1$  and  $B_2$  are constants. For the case of manganese the term in  $Z^2 \lambda_m^3$  due to Rayleigh scattering contributes significantly to the observed ratio and thus reduces the size of the relative resonance effect. The term in  $Z^2 \lambda_m^3$  also introduces a non-resonant variation with  $\lambda_m$  in the observed ratio  $R_e(\lambda_m)/R_i(\lambda_m)$ . After correcting for this effect as discussed in Appendix V we find the results shown in Fig. 13. The figure shows the corrected ratio  $[R_e(\lambda_m)/R_i(\lambda_m)]_{\text{corrected}}$  as a function of the monochromator setting  $\lambda_m$ . The curve shown on the figure is the result of a least-square fit of Eq. 34 to the data. From the least-square fit the parameters in the equation were found to be

$$\begin{aligned}
 a_1 &= (1.464 \pm 0.003)10^{-2}, & a_2 &= (2.8 \pm 0.4)10^{-4}, \\
 \tau &= 0.205 \pm 0.027 \text{ x-units}, & \lambda_T &= 98.233 \pm 0.008 \text{ x-units}.
 \end{aligned}
 \tag{45}$$

Some typical counting rates observed in the experiment are given in the following table:

	Monochromator Wavelength Position	
	98.233 x-units	97.951 x-units
$R_e(\lambda_m)$	$79.9 \pm 0.3 \frac{\text{counts}}{\text{minute}}$	$78.6 \pm 0.3 \frac{\text{counts}}{\text{minute}}$
$R_i(\lambda_m)$	5,337 "	5,362 "

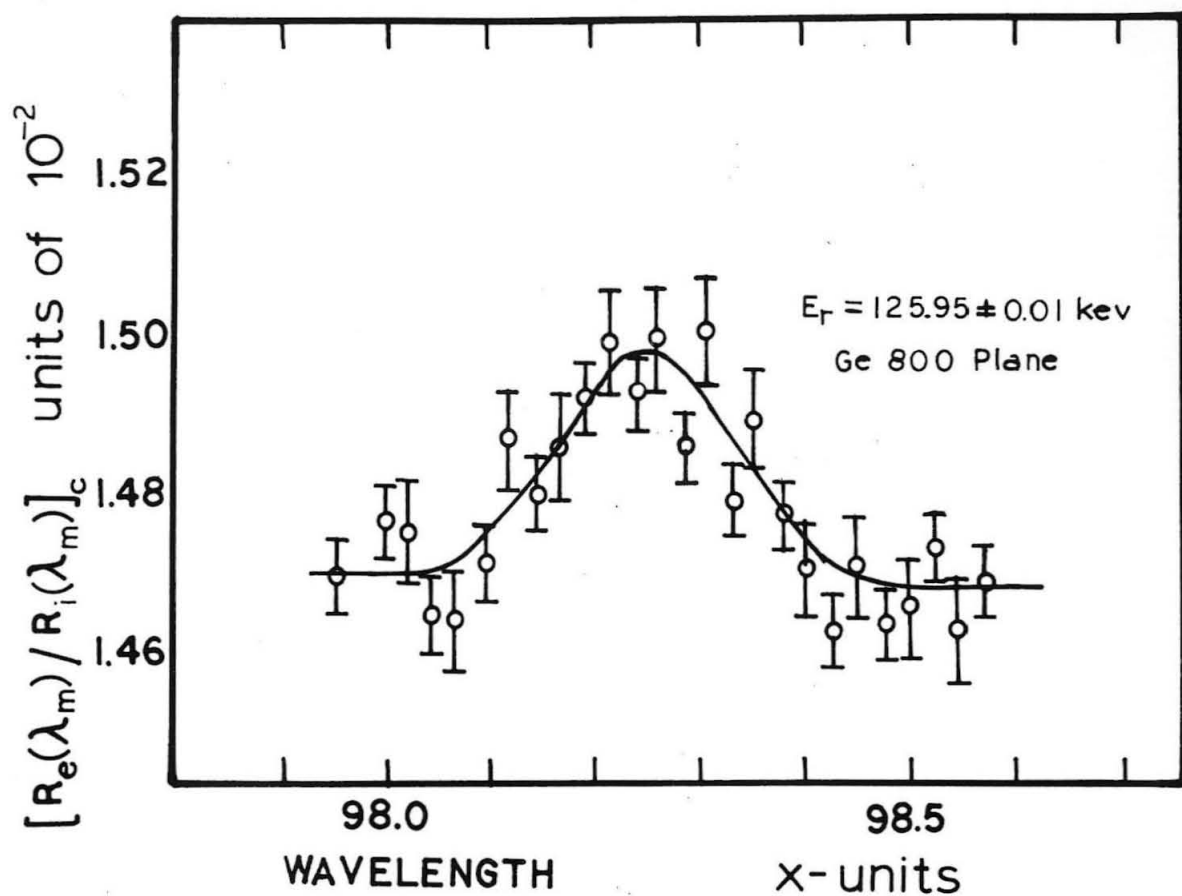


Fig. 13. Nuclear-resonance excitation of the first-excited state in  $Mn^{55}$  observed with a germanium-diffraction crystal in the monochromator. The figure shows the corrected ratio of the elastic to the inelastic radiation from a manganese sample as a function of the wavelength of the incident beam.

From the value of  $\lambda_r$  given above, the resonance position was found to be

$$E_r = 125.95 \pm 0.01 \text{ kev.} \quad (46)$$

Proceeding as described in the analysis of the lithium fluoride experiment one, the resonance width for the 125.95 kev level in  $\text{Mn}^{55}$  was found from Appendix II, Table VI to be

$$\Gamma = (1.1 \pm 0.3)10^{-6} \text{ ev.} \quad (47)$$

#### IV. FINAL RESULTS AND CONCLUSIONS

The final results on the fluorine resonance are obtained by taking weighted averages of the results of the scattering experiments on lithium fluoride given in Eqs. 36 and 43 for the resonance energy position and Eqs. 39, 41, and 44 for the resonance energy width. From these we find for the first-excited state of  $\text{F}^{19}$

$$\begin{aligned} E_r &= 109.894 \pm 0.005 \text{ kev;} \\ \Gamma &= (5.1 \pm 0.7)10^{-7} \text{ ev or } \tau_{\frac{1}{2}} = (0.9 \pm 0.1)10^{-9} \text{ sec} \end{aligned} \quad (48)$$

where  $\tau_{\frac{1}{2}}$  is the half-life of the state. The resonance-energy value obtained is in good agreement with result  $E_r = 109.87 \pm 0.04 \text{ kev}$  obtained by Chupp, DuMond, Gordon, Jopson, and Mark (35) in some Coulomb-excitation experiments with a bent-crystal spectrometer. The resonance half-life obtained can be compared with the value  $(1.0 \pm 0.25)10^{-9} \text{ sec}$  which was obtained by Thirion, Barnes, and Lauritsen (36) in a Coulomb-excitation experiment.

The final results for the  $\text{Mn}^{55}$  resonance energy and width are given by Eqs. 46 and 47:

$$\begin{aligned} E_r &= 125.95 \pm 0.01 \text{ kev;} \\ \Gamma &= (1.1 \pm 0.3)10^{-6} \text{ ev or } \tau_{\frac{1}{2}} = (0.4 \pm 0.1)10^{-9} \text{ sec.} \end{aligned} \quad (49)$$

Chupp et al. (35) also measured the energy of this level. They found  $E_r = 125.87 \pm 0.05$  kev for the resonance energy. Using fast timing techniques Holland and Lynch (37) have measured the half-life of this level to be  $(0.34 \pm 0.10)10^{-9}$  sec. The B(E2) transition probability of this level in manganese has been measured by Temmer and Heydenburg (38). From their result the E2 half-life is calculated to be  $4.8 \times 10^{-8}$  sec. Comparing this with our result one obtains 0.8 percent for the ratio between the intensities of E2 and M1 radiation. This is in agreement with angular correlation measurements by Bernstein and Lewis (39) which indicate that the value of this ratio is less than two percent.

The results obtained in this experiment through the technique of nuclear excitation with a diffracted x-ray beam are in good agreement with those obtained through other techniques. As can be seen from the results this method gives a precise determination of the energy position of the levels which are excited. In the determination of resonance widths the accuracy obtained in this experiment was limited by the available intensity in the incident diffracted beam and by background from atomic scattering in the sample.

In conclusion we comment on experimental work required for the future application of this technique of nuclear excitation. The observations made here indicate two general directions in which further work is required. (i) Experimental work directed towards increasing the intensity and resolution of the incident diffracted beam. This might be attained through the use of larger diffraction

crystals in the monochromator and through the use of a more intense x-ray source. (ii) A second problem which needs to be solved is that resulting from the background coming from electronic scattering in the sample. Rayleigh scattering from the atomic electrons places a severe restriction on the size of the nuclear scattering effect which can be observed. This problem might be solved by taking advantage of the instantaneous character of atomic scattering as compared to the life time of the nuclear states excited. Through the use of a pulsed x-ray beam and a properly gated detector it should be possible to observe only the nuclear excitation events in the sample.

**APPENDICES**

## APPENDIX I

### MECHANICAL DESIGN OF THE MONOCHROMATOR

Many considerations leading to the design of the present monochromator are similar to considerations discussed in references 1 and 40. Practical requirements such as the availability of two-meter-radius curved-crystal clamping-blocks, length, pitch and precision of lead screws available, the optimum lever arm length to allow large angular magnification with a minimum of bending, determined the over-all dimensions of the instrument. With these proportions established an analysis of all calculable mechanical errors was made. Each error was to be limited to  $\pm 0.001$  s.d. which corresponds to 0.001 x-units in wavelength resolution for the quartz (310) planes. The design we have finally adopted is illustrated in Fig. 1.

#### A. Design of Crystal-Pivot Unit

The crystal-pivot bearing, lever arm, and sine-screw assembly is mounted on an octahedron constructed of welded square steel tubing, provided with three leveling screws. The pivot shaft, shown in Fig. 14, is ground and lapped and rotates in two "Oilite" bearings. The inside diameter of each bearing is first fitted accurately to the pivot shaft then milled out leaving two narrow strips,  $90^\circ$  apart, as shown in the insert in Fig. 14. A wedge bottom groove is machined opposite the two strips. A bronze spring with a mating wedge projection is inserted in the groove. The spring has two strips that are machined to a slightly larger radius than the pivot shaft. A "T" slot in the

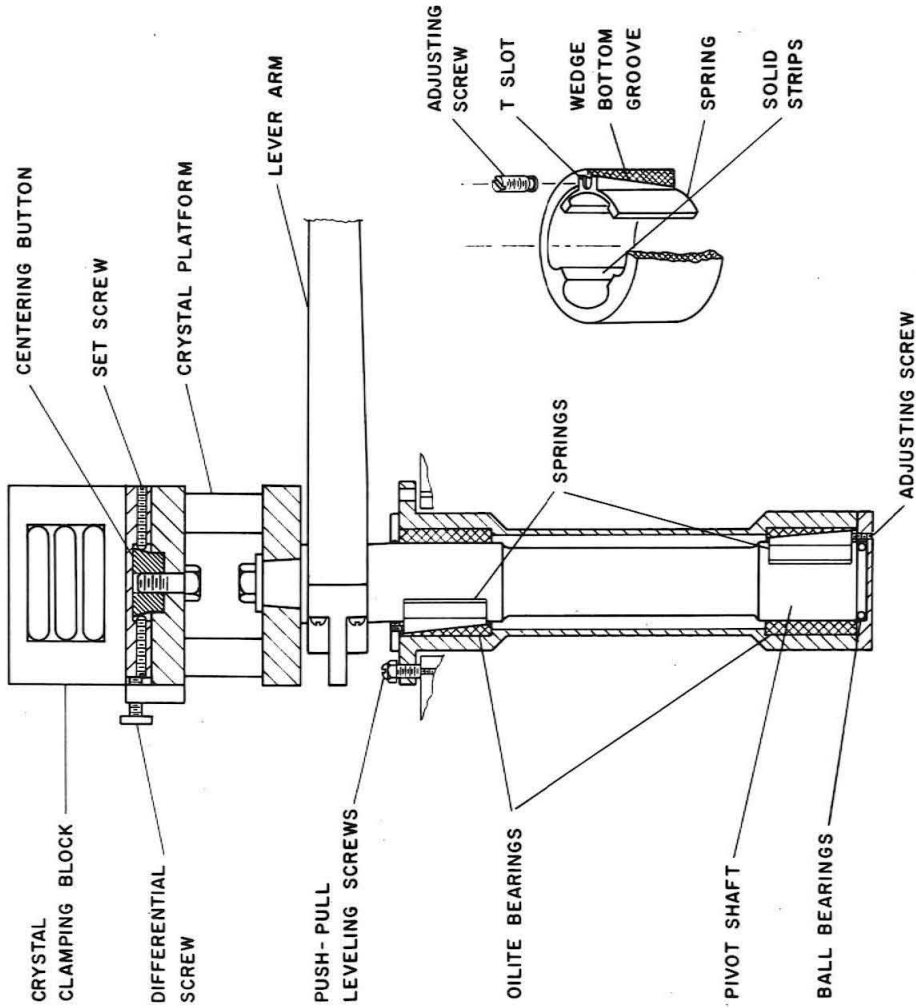


FIG. 14. Line drawing of the pivot-bearing assembly showing the pivot shaft with the crystal clamping-block and lever arm. The insert gives the details of the "Oilite" bearings designed to provide a uniform bearing pressure on the pivot shaft.

top of the spring is engaged by a button on the adjusting screw which raises or lowers the spring thus decreasing or increasing the bearing pressure on the pivot shaft. The two bearings are mounted  $180^{\circ}$  from each other so that the moment, due to the weight of the lever arm, is taken up by the solid strips of both "Oilite" bearings. The axial thrust of the pivot shaft is carried by a ring of ball bearings. The whole pivot assembly is enclosed in an oil filled housing with a felt dust seal at the top.

The crystal-block-mounting assembly consists of four parts. The convex crystal clamping-block is screwed to the upper plate shown in Fig. 14 . The upper plate is provided with a large hole which clears the conical portion of the centering button. Four radial set screws in the upper plate clamp the centering button allowing small adjustments in the horizontal plane. The cylindrical end of the centering button pivots in a bored hole in the crystal platform. A differential screw, mounted on the platform, provides small rotational adjustment of the upper plate. The lower part of the platform is fitted to a taper on the main pivot shaft and clamped with a cap screw.

The lever arm is clamped rigidly to the main pivot shaft. In the horizontal plane the lever is parabolic in shape to achieve maximum rigidity with minimum weight.

The sine-screw mechanism is shown in Fig.15 with one bearing plate and cheek plate removed for clarity. Figure 16 shows a photograph of the sine-screw unit. The precision ground and lapped lead screw engages a bronze split nut. End thrust on the lead screw is borne by a hardened and polished spherical button bearing against a

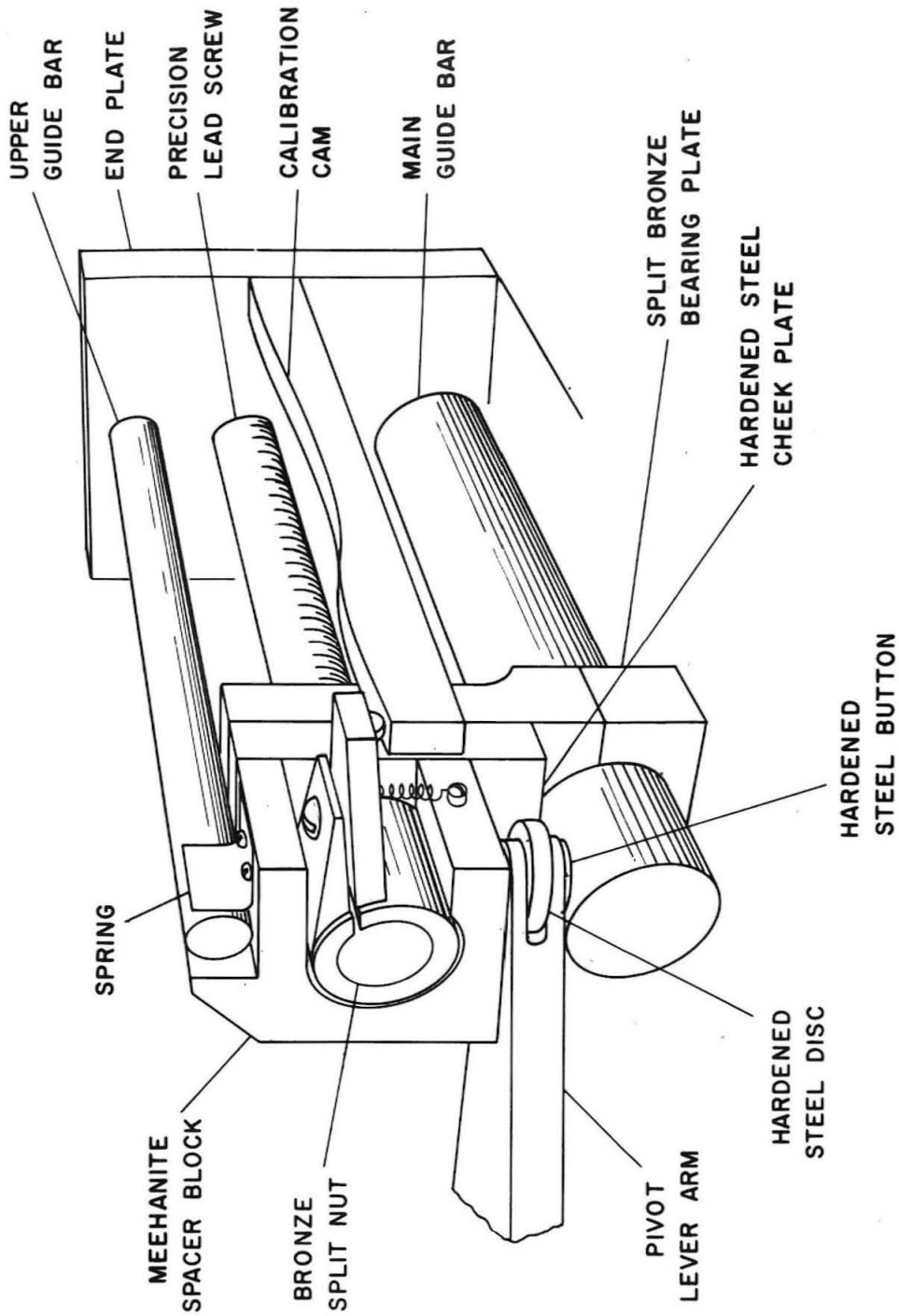


Fig. 15. Line drawing illustrating the sine-screw mechanism.

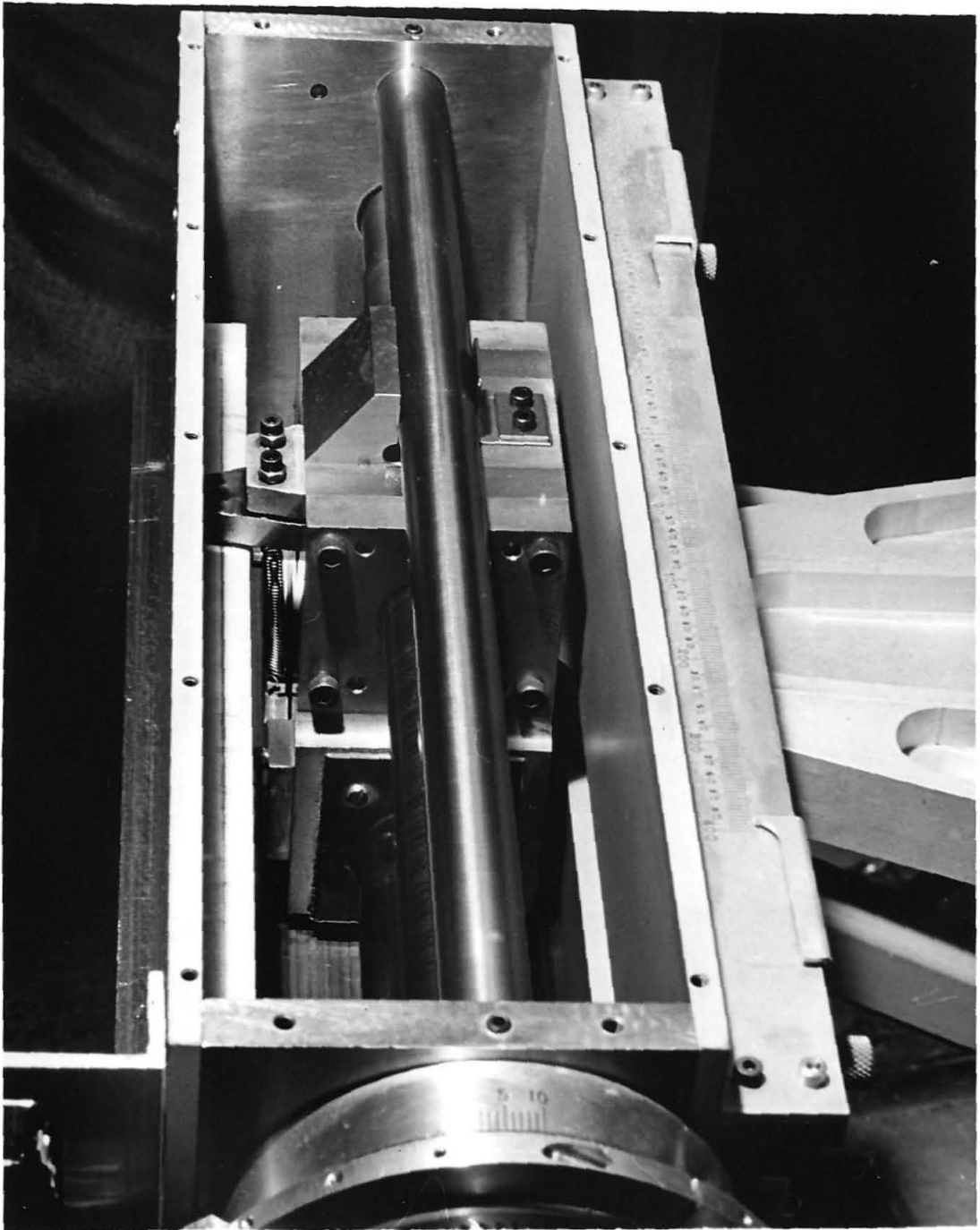


Fig. 16. Photograph of the sine-screw mechanism with a cover plate removed. The upper guide-bar, precision lead-screw, and main guide-bar can be seen. Also seen is the radial projection from the bronze split-nut held to ride on the calibration cam by the spring.

flat hardened plate, not shown in the figure. The bronze split nut has an adjusting screw to achieve proper thread contact. Part of the split nut projects radially and is fitted with a small roller which rides on the calibration cam. When the lead screw is rotated clockwise the calibration cam constrains the split nut in the tangential direction. If the contact surface of the cam were straight the axial motion of the split nut would be determined only by the pitch of the lead screw. However, as shown in Fig. 15, the cam is profiled to correct for nonlinearities in the pitch of the lead screw. As the split nut projection rides along the cam the profiled surface imparts additional rotation to the split nut that appropriately adds to or subtracts from the pitch of the lead screw. The total correction range of the cam is equivalent to 0.1 x-units of gamma-ray wavelength.

Straddling the split nut is the sliding assembly provided with two split bronze bearing plates that slide on the main guide bar. A projection on the "Meehanite" spacer block is held against the upper guide bar by a flat spring. The sliding assembly clears the lead screw and is constrained to move in a straight line by the two guide bars. The ends of the bronze split nut are polished flat and contact two hardened and polished cheek plates. These plates extend down to contact a hardened and polished steel disc which is clamped in the end of the pivot lever arm.

The pressure on the main pivot bearings, seen in Fig. 14, is partially relieved by providing a hardened and polished button, at the end of the lever, which rides on the main guide bar.

The pitch of the lead screw is such that the crystal pivots through 3 minutes of arc per turn. One-half turn is denoted as one 'screw division' (s.d.). When using the (310) planes of quartz as the diffraction crystal one screw division is exactly equal to one x-unit of wavelength. A revolution counter and a vernier dial on the lead screw give direct readings to 0.001 s.d.

Precision stepwise motion of 0.02 s.d. per step is obtained by using a solenoid actuated pall to drive a 100-tooth ratchet wheel attached directly to the lead screw. A direct current motor provides rapid motion from one setting to another. This motor is automatically disengaged when not running.

#### B. Design of Detector Carriage

The collimator and detector are mounted on a platform which rides on a circular track assembly shown in Fig. 1. The platform must rotate about a center which coincides with the crystal-pivot bearing through twice the angle of rotation of the crystal. The top of the outer track is machined to form a  $90^\circ$  triangular cross-section. The platform is fitted with two pairs of ball bearings that ride on the two  $90^\circ$  faces of the outer track constraining the platform to rotate in a circle. The two inner bearings, close to the pivot, are conical and ride on a conical rail whose apexes coincide at the crystal pivot. This is to allow the platform to roll with a minimum of sliding friction. The unit is designed to carry a 6,000 lb. load.

The position of the collimator and detector relative to the crystal is not, of course, related to the precision of the instrument but affects only the intensity of the transmitted gamma-ray beam. The collimator presently used is 18 inches long consisting of 29 stainless steel strips, 0.016 inch thick and 2 inches high. Each sheet is clad on both sides with 0.002 inch thick lead foil. The tapered openings measure 0.050 inch at the entrance end and 0.061 inch at the exit. With this collimator an error in the position of the collimator and detector platform at the outer rail of 0.010 inch results in a 3 percent decrease in the intensity of the transmitted beam. With this in mind the following simple tracking solution was used.

A square groove was machined in the outer track to accommodate a curved rack which meshes with a spur gear driven by a selsyn motor attached to the carriage. The motor is coupled to a selsyn generator whose rotor is connected to the lead screw of the sine-mechanism. Since the rotation of the lead screw is proportional to the sine of the crystal rotation  $\nu$  and the spur gear and rack mechanism is proportional to  $\nu$  a linear rack would introduce an error of 0.1 inch at each end of the travel. A special rack was cut with a gradual increase in tooth spacing to correspond to the difference between  $\nu$  and  $\sin \nu$  as  $\nu$  increased from 0 to  $\pm 18^\circ$ . The greatest deviation of tooth spacing from normal pitch was 0.002 inch, which is less than the normal allowance for back lash (0.003 inch) of commercial gears.

APPENDIX II

DETERMINATION OF NUCLEAR RESONANCE WIDTH USING A SCATTERING SAMPLE OF ARBITRARY THICKNESS

Here we obtain the expression used to evaluate  $B(\square)$  in Eq. 33 and present tables of this function which were used to analyze the experimental results. The procedure used to relate the experimentally observed quantity  $R_n(E_m)/R_c(E_m)$  to the resonance width is similar to that used in the thin sample approximation given in Chapter III (A).

For the case of a scattering sample of thickness  $L$  the counting rate  $R_n(E_m)$  due to nuclear scattering is (compare Eq. 22)

$$R_n(E_m) = CN \int_{-\infty}^{+\infty} dE \int_0^L dx \left[ \sigma_n(E) \phi(E-E_m) \exp-Nx \left( \sigma_e(E) + \sigma_n(E) \right) \cdot \exp-Nx \left( \sigma_e(E) + \sigma_n(E) \right) / |\cos \xi_0| \right] \quad (50)$$

where  $\xi_0$  is the average scattering angle and  $\sigma_e(E)$  and  $\sigma_n(E)$  are respectively the electronic and nuclear interaction cross sections. The first exponential factor in the equation gives the attenuation of the photon intensity which arrives at the position  $x$  in the target. The second exponential factor gives the attenuation of the scattered photon intensity resulting from scattering in  $dx$  which arrives at the detector. We integrate Eq. 50 over  $x$  and note that since  $\phi(E-E_m)$  and  $\sigma_e(E)$  are slowly varying functions of  $E$  in comparison to  $\sigma_n(E)$  we can substitute their values for  $E$  equal to  $E_r$ .

Then Eq. 50 becomes

$$R_n(E_m) = C\phi(E_r - E_m) \int_{-\infty}^{+\infty} \frac{dE \sigma_n(E) [1 - \exp(-NL) (\sigma_e(E_r) + \sigma_n(E)) (1 + 1/\cos|\xi_o|)]}{(\sigma_e(E_r) + \sigma_n(E)) (1 + 1/|\cos \xi_o|)}, \quad (51)$$

As for the case of a thin scattering sample we notice that

$$\phi(E - E_r) \propto R_n(E). \quad (52)$$

Now we obtain the expression for the counting rate  $R_c(E_m)$  resulting from Compton scattering. This is given by (compare Eq. 25)

$$R_c(E_m) = CNZ \int_{-\infty}^{+\infty} dE \int_0^L dx \left[ \sigma_c(E) \phi(E - E_m) \exp(-Nx) (\sigma_e(E) + \sigma_n(E)) \cdot \exp(-Nx) (\sigma_e(E') + \sigma_n(E')) / |\cos \xi_o| \right] \quad (53)$$

where  $E'$  is the energy of Compton scattered photons given by Eq. 19 with  $\xi$  equal to  $\xi_o$ . This equation is integrated over  $x$ . Then since  $\sigma_c(E)$ ,  $\sigma_e(E)$ , and  $\sigma_e(E')$  are slowly varying functions of  $E$  compared to  $\phi(E - E_m)$ , we can replace them by  $\sigma_c(E_m)$ ,  $\sigma_e(E_m)$ , and  $\sigma_e(E'_m)$ . Also we can replace  $\sigma_n(E)$  and  $\sigma_n(E')$  by zero without introducing significant error to the value of the integral.

Then Eq. 53 becomes

$$R_c(E_m) = \frac{CZ \sigma_c(E_m) [1 - \exp(-NL) (\sigma_e(E_m) + \sigma_e(E'_m)) / |\cos \xi_o|]}{\sigma_e(E_m) + \sigma_e(E'_m) / |\cos \xi_o|} \int_{-\infty}^{+\infty} \phi(E - E_m) dE. \quad (54)$$

From Eqs. 51, 52, and 54

$$\int_{-\infty}^{+\infty} \frac{R_n(E) dE}{R_c(E_r)} = A(\square) \quad (55)$$

where

$$A(\Gamma) = \frac{\int_{-\infty}^{+\infty} dE \sigma_n(E) \left[ 1 - \exp(-NL \left( \sigma_e(E_r) + \sigma_n(E) \right) \left| 1 + 1/|\cos \xi_o| \right| \right)}{\left| \sigma_e(E_r) + \sigma_n(E) \right| \left| 1 + 1/|\cos \xi_o| \right|} \cdot \frac{Z \sigma_c(E_r) \left[ 1 - \exp(-NL \left( \sigma_e(E_r) + \sigma_e(E'_r) / |\cos \xi_o| \right)) \right]}{\sigma_e(E_r) + \sigma_e(E'_r) / |\cos \xi_o|} \quad (56)$$

The above expression for  $A(\Gamma)$  becomes a function of  $\Gamma$  when Eq. 17 is substituted for  $\sigma_n(E)$ .

Eq. 55 reduces to Eq. 29 in the limit of small thickness  $L$ . There are two interesting limits for the case of a thick foil. First, suppose that  $NL\sigma_e(E_r) \gg 1$  and  $\sigma_e(E_r) \gg \sigma_n(E_r)$  then Eq. 55 gives

$$\Gamma = \frac{2Z\sigma_c(E_r)}{\pi\sigma_o} \cdot \frac{\sigma_e(E_r) \left[ 1 + 1/|\cos \xi_o| \right]}{\sigma_e(E_r) + \sigma_e(E'_r) / |\cos \xi_o|} \cdot \frac{\int_{-\infty}^{+\infty} R_n(E) dE}{R_c(E)} \quad (57)$$

Now consider the case  $NL\sigma_e(E_r) \gg 1$  where  $\sigma_e(E_r) = \sigma_n(E_r)$ . In this case Eq. 55 gives

$$\Delta = \frac{0.93Z\sigma_c(E_r) \left[ 1 + 1/|\cos \xi_o| \right]}{\sigma_e(E_r) + \sigma_e(E'_r) / |\cos \xi_o|} \cdot \frac{\int_{-\infty}^{+\infty} R_n(E) dE}{R_c(E_r)} \quad (58)$$

indicating that for this case the size of the observed effect is determined by the Doppler width rather than nuclear-resonance width.

Eq. 55 is an implicit equation from which the nuclear-resonance width is determined from the observed experimental results. In the analysis of the data the right side of the equation was numerically

determined for each scattering sample as a function of  $\Gamma$ . The value of  $\Gamma$  corresponding to the experimental results for the left side of the equation gives the nuclear-resonance width.

In the determination of  $\Gamma$  from the experimental data it is convenient to use (see Eq. 33)

$$B(\Gamma) = 1.065 \frac{\lambda_r}{E_r} A(\Gamma). \quad (59)$$

Tables V and VI give calculated values of  $B(\Gamma)$  versus  $\Gamma$  for the lithium fluoride and manganese samples used in the experiment.

TABLE V. Tabulation of  $B(\Gamma)$  for lithium fluoride scattering sample.

Resonance Width $\Gamma$ ev	$B(\Gamma)$ x-units	Resonance Width $\Gamma$ ev	$B(\Gamma)$ x-units
$0.5 \times 10^{-7}$	$0.27 \times 10^{-5}$	$5.5 \times 10^{-7}$	$2.90 \times 10^{-5}$
1.0	0.53	6.0	3.16
1.5	0.79	6.5	3.42
2.0	1.06	7.0	3.68
2.5	1.32	7.5	3.95
3.0	1.59	8.0	4.21
3.5	1.85	8.5	4.47
4.0	2.11	9.0	4.73
4.5	2.38	9.5	4.99
5.0	2.64	10.0	5.25

TABLE VI. Tabulation of  $B(\Gamma)$  for manganese scattering sample.

Resonance Width $\Gamma$ ev	$B(\Gamma)$ x-units	Resonance Width $\Gamma$ ev	$B(\Gamma)$ x-units
$1.0 \times 10^{-7}$	$0.29 \times 10^{-5}$	$1.1 \times 10^{-6}$	$3.16 \times 10^{-5}$
2.0	0.58	1.2	3.45
3.0	0.87	1.3	3.73
4.0	1.16	1.4	4.01
5.0	1.45	1.5	4.29
6.0	1.74	1.6	4.57
7.0	2.02	1.7	4.85
8.0	2.31	1.8	5.13
9.0	2.59	1.9	5.40
10.0	2.88	2.0	5.68

APPENDIX III

CORRECTIONS APPLIED TO MANGANESE AND FLUORINE DATA

Through the factor  $\delta$  introduced in Eq. 30 correction was applied to the data for: (1) variation in detector efficiency with incident photon energy (denoted as  $\delta_1$ ), (2) anisotropy in the Compton scattering (denoted as  $\delta_2$ ), (3) anisotropy in the nuclear scattering (denoted as  $\delta_3$ ), (4) multiple scattering of photons in the scattering sample (denoted as  $\delta_4$ ). The amounts of the corrections applied for each of these effects are given in the following table:

Scattering Sample	$\delta_1$	$\delta_2$	$\delta_3$	$\delta_4$	$\delta = \delta_1 \delta_2 \delta_3 \delta_4$
LiF	1.03	0.87	1.00	1.18	1.05
Mn	1.06	0.85	0.99	1.22	1.09

The correction term  $\delta_1$  was determined from the calculated efficiency of NaI crystals of Wolicki, Jastrow, and Brooks (41). The  $\delta_1$  term is obtained by taking the ratio of the NaI-crystal efficiency for photons at the Compton scattered energy to the NaI-crystal efficiency for photons at the incident energy.

The correction term  $\delta_2$  for asymmetry in the Compton scattering was determined using Eqs. 20 and 21 from the formula

$$\delta_2 = \frac{4\pi [d\sigma_c/d\Omega]_{\xi}}{\sigma_c} = \xi_0 \quad (60)$$

The correction term  $\delta_3$  for asymmetry in the nuclear scattering can be determined from the theory of angular correlation of nuclear radiation (42). The correction depends on the angular momentum of the initial and excited states and the multipolarity and mixing ratios of the transitions. For  $F^{19}$  the angular distribution is isotropic, and therefore  $\delta_3 = 1.00$ . For  $Mn^{55}$  the angular distribution is not well determined because of an uncertainty in the mixing ratio. However, angular distribution measurements of the 126 keV gamma-rays emitted following Coulomb excitation by alpha particles have been measured by Bernstein and Lewis (39). From their experimental results the correction factor  $\delta_3$  was estimated to be 0.99.

In the derivation of Eqs. 29 and 55 the effect of multiple scattering events in which a photon arrives at the NaI detector after two or more scattering events, was neglected. For a thin scattering sample this effect is negligible, but for a thick sample the effect can become rather large. For the experiment with the lithium fluoride scattering sample an experimental determination and also a calculated estimate of  $\delta_4$  were made. The experimental determination was obtained through the following procedure. A thin lithium fluoride scattering sample was placed in the incident beam, and the counting rate of the inelastic scattering channel was observed as a function of the position of the sample with respect to the detector. Analysis of this data in comparison with the counting rate observed with the thick lithium fluoride scattering sample in place gives the value of the correction  $\delta_4 = 1.18$ .

A calculated estimate of  $\delta_4$  was made and found to be 1.24 for lithium fluoride scattering sample and 1.22 for the manganese sample. The calculated value was used to correct the manganese experiment.

APPENDIX IV

ANALYSIS OF THE INTENSITIES OBSERVED IN THE ELASTIC  
AND INELASTIC COUNTING CHANNELS

Here we obtain the expression given in Eq. 37 for evaluation the ratio  $R_n(E_r)/R_c(E_r)$  from the experimental data. We also give a detailed description of the method used in the experiment to determine the efficiency factors  $\epsilon_e$  and  $\epsilon_i$  and the quantity in the brackets of Eq. 37.

Eq. 37 was derived in the following manner. The counting rate  $R_e(\lambda_m)$  observed in the elastic channel is the sum of three terms;

$$R_e(\lambda_m) = \epsilon_e R_n(E_m) + R_A(\lambda_m) + R_e^{bgd}(\lambda_m) \quad (61)$$

where  $\epsilon_e R_n(E_m)$  is the contribution to  $R_e(\lambda_m)$  resulting from nuclear scattering,  $R_A(\lambda_m)$  is the contribution from scattering by the atomic electron (see Appendix V), and  $R_e^{bgd}(\lambda_m)$  is the crystal-background counting-rate present when the diffracted beam is not incident on the scattering sample. Similarly the counting rate in the inelastic counting channel is given by

$$R_i(\lambda_m) = \epsilon_i R_c(E_m) + R_i^{bgd}(\lambda_m) \quad (62)$$

where  $\epsilon_i R_c(E_m)$  is the contribution to  $R_i(\lambda_m)$  resulting from Compton scattering and  $R_i^{bgd}(\lambda_m)$  is the crystal-background counting-rate. In the experiment the crystal-background counting-rates were observed by setting the crystal to the position  $(\lambda_m - 10.000)$  x-units with the collimator at the position corresponding to  $\lambda_m$ . Under these

conditions the diffracted beam cannot pass through the collimator to the scattering sample. Placing Eq. 31 into Eq. 61 and using Eq. 62 gives

$$\frac{R_e(\lambda_m)}{R_i(\lambda_m)} = \frac{R_A(\lambda_m) + R_e^{bgd}(\lambda_m) + \epsilon_e R_n(E_r) \exp-2.773[(\lambda_m - \lambda_r)/\tau]^2}{\epsilon_i R_c(E_m) R_i(\lambda_m) / [R_i(\lambda_m) - R_i^{bgd}(\lambda_m)]} \quad (63)$$

This equation is the basis for Eq. 34 which was used in the least-square analysis of the experimental data. The variation in  $R_e(\lambda_m)/R_i(\lambda_m)$  with  $\lambda_m$  resulting from changes in the non-resonance terms of Eq. 63 is negligibly small in the experiment with the lithium fluoride scattering sample. The effect of these terms in the experiment with the manganese scattering sample is discussed in Appendix V. Comparing Eq. 63 with Eq. 34 we obtain

$$\frac{R_n(E_r)}{R_c(E_r)} = a_2 \frac{\epsilon_i}{\epsilon_e} \left[ \frac{R_i(\lambda_r)}{R_i(\lambda_r) - R_i^{bgd}(\lambda_r)} \right] \quad (64)$$

which is the expression given in Eq. 37 .

The efficiency factors  $\epsilon_i$  and  $\epsilon_e$  and the quantity in the brackets were determined for each experiment from data taken preceding and following collection of data for the points in Figs. 9 and 12 for lithium fluoride and Fig. 13 for manganese. The efficiency factor  $\epsilon_i$  was determined from the equation

$$\epsilon_i = \frac{R_i(\lambda_r) - R_i^{bgd}(\lambda_r)}{I_i(\lambda_r) - I_i^{bgd}(\lambda_r)} \quad (65)$$

where  $I_i(\lambda_r)$  is the integrated counting rate of the pulse spectrum similar to that given in Fig. 8, and  $I_i^{bgd}(\lambda_r)$  is the integrated counting rate of the pulse spectrum obtained when the monochromator crystal is in the crystal background position. In Eq. 65 the values of  $R_i(\lambda_r)$  and  $R_i^{bgd}(\lambda_r)$  were observed simultaneous to the observation of the pulse spectrum measurements. Also from these values the factor in the brackets in Eq. 64 was determined. A formula identical to Eq. 65 with  $i$  replaced by  $e$  was used to obtain  $\epsilon_e$ . In this case the single-channel pulse-height-analyzer counting-rate and the pulse spectrum from the "Penco" 100-channel analyzer were determined with the detector placed directly in the diffracted beam of the monochromator.

APPENDIX V

CORRECTION FOR RAYLEIGH SCATTERING EFFECTS IN THE  
MANGANESE EXPERIMENT

In Fig. 17 the observed ratio  $R_e(\lambda_m)/R_i(\lambda_m)$  for the manganese scattering sample is shown as a function of wavelength of the incident beam. The sloping base line seen in the figure primarily results from non-resonant variation of  $R_e(\lambda_m)$  due to elastic scattering by the atomic electrons (Rayleigh scattering). A correction linear in  $\lambda_m$  was applied to the data in Fig. 17 to obtain the results presented in Fig. 13. We here discuss the effect of Rayleigh scattering in resonance-excitation experiments and then derive the equation (Eq. 70 below) used to correct the manganese data.

To understand the non-resonant variation in  $R_e(\lambda_m)/R_i(\lambda_m)$  each of the non-resonant terms in Eq. 63 were investigated. Results of the investigation indicate that the most significant term is  $R_A(\lambda_m)$ , the counting rate due to scattering by the atomic electrons. This term is the sum of a contribution resulting from Compton scattered photons and a contribution resulting from Rayleigh scattered photons. To investigate the relative magnitude of these two factors, pulse spectrums were observed using scattering samples of various atomic number. Fig. 18 shows pulse spectra (corrected for background) obtained with a beam of 125.00 kev photons incident on the scattering samples. In the measurements thin scattering samples were used. The pulse spectra in Fig. 18 have been normalized to

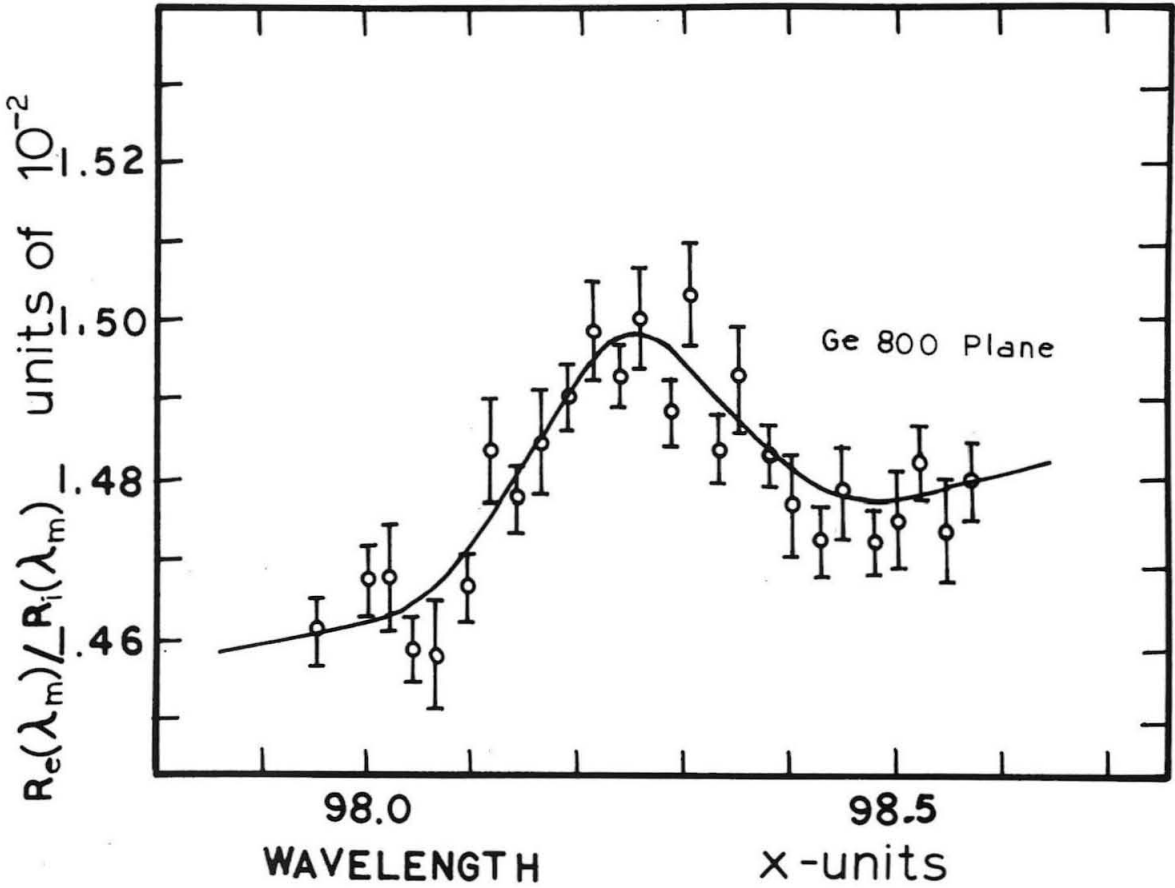


Fig. 17. Nuclear-resonance excitation of the first-excited state in  $Mn^{55}$  observed with a germanium-diffraction crystal in the monochromator. The figure shows the ratio of the elastic to the inelastic radiation from a manganese sample as a function of the wavelength of the incident beam.

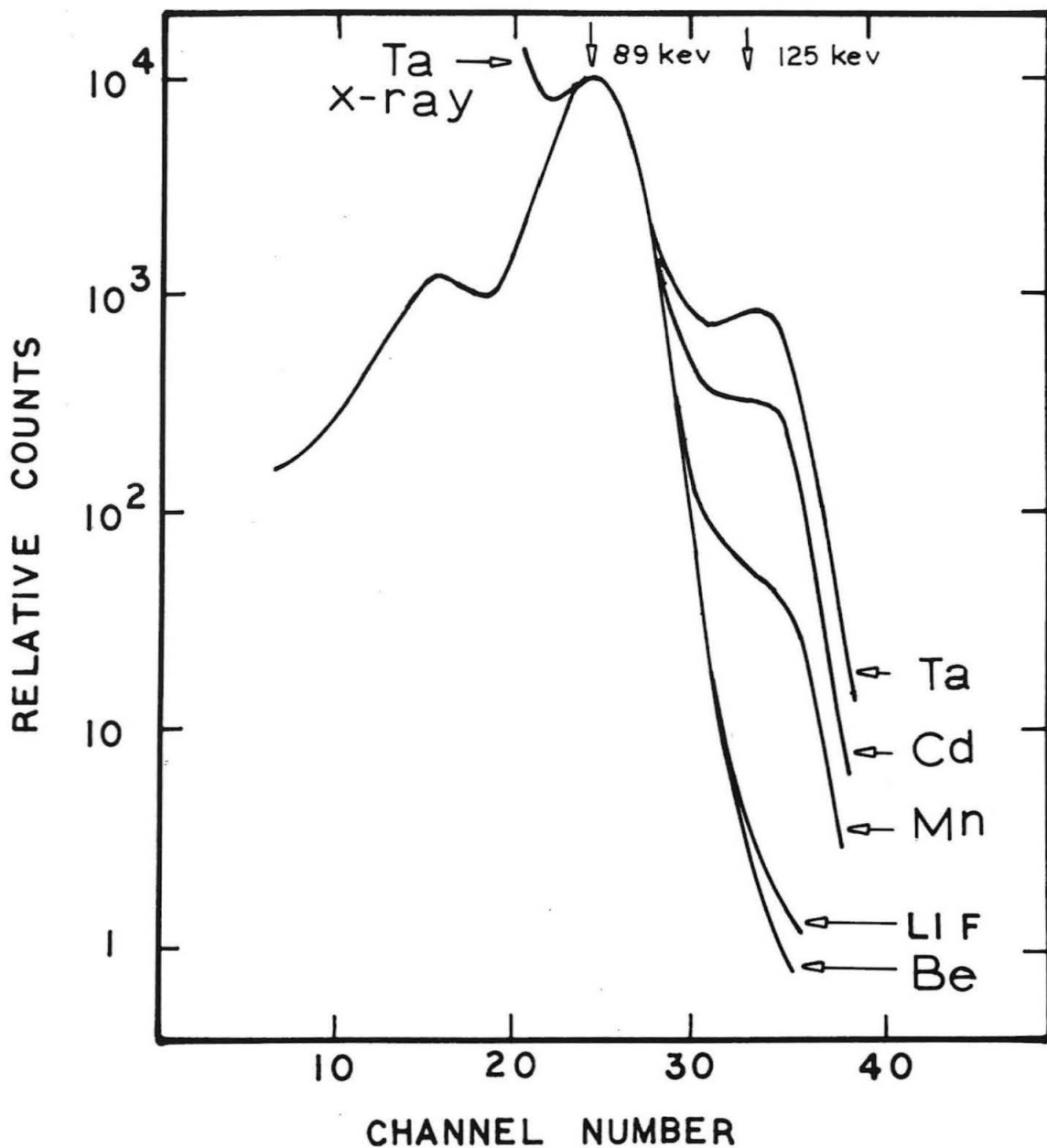


Fig. 18. Pulse spectra observed from the NaI detector resulting from scattering of 126.00 keV incident photons by scattering samples of various composition.

show the spectrum which would be obtained from a scattering sample of thickness such that  $NL \sigma_c(E) = 0.05$ .

In Fig. 18 the large peak at 89 keV is due to Compton scattering in the samples. For each sample the integrated counting rate under this peak is given by Eq. 26. The peak at 125 keV, which is most clearly observed in the scattering from tantalum, is due to Rayleigh scattering in the samples\*. For a thin sample the integrated counting rate under the Rayleigh peak is given by an equation similar to Eq. 26

$$R_R(E_m) = CNL \sigma_R(E_m) \int_{-\infty}^{+\infty} \phi(E-E_m) dE \quad (66)$$

where  $\sigma_R(E_m)$  is the cross section for Rayleigh scattering. Franz (43) has derived an approximate formula for the Rayleigh-scattering cross section

$$\sigma_R(E) = \frac{8.67 \times 10^{-33}}{\sin^3(\xi/2)} \left( \frac{mc^2 Z}{E} \right)^3 \frac{1 - \cos^2 \xi}{2} \frac{\text{cm}^2}{\text{ster}} \quad (67)$$

where  $Z$  is the atomic number. Several authors (44, 45) have discussed this formula. They find that the dependence of the cross section on the atomic number and incident energy given by  $(Z/E)^3$  is approximately correct. To the precision of the experiment we have observed the  $(Z/E)^3$  variation in the elastic peak of pulse-spectra measurements similar to those in Fig. 18 at various incident energies from 110 keV and 150 keV.

\* Thomson nuclear scattering yields a negligible contribution to the elastic scattering. The cross section for this process is  $\sigma_T(E) = 1.19 \times 10^{-32} (1 + \cos^2 \xi) (Z^2/A)^2 \text{ cm}^2/\text{ster}$ .

We now use these results to obtain the correction formula which was applied to the manganese data given in Fig. 17. In the manganese experiment the elastic-counting channel is set to observe pulses in the region of channels 33 to 37. The counting rate  $R_A(\lambda_m)$  in this region can be written as the sum of a term proportional to  $R_c(E_m)$  and a term proportional to  $R_r(E_m)$ . Therefore, from Eqs. 26 and 66 we expect the wavelength dependence of  $R_A(\lambda_m)/R_c(E_m)$  to be given by

$$R_A(\lambda_m)/R_c(E_m) = B_1 + B_2 Z^2 \lambda_m^3 \quad (68)$$

where  $B_1$  and  $B_2$  are constants. Expanding near the nuclear resonance wavelength  $\lambda_r$  gives

$$\frac{R_A(\lambda_m)}{R_c(E_m)} \approx \frac{R_A(\lambda_r)}{R_c(E_r)} \left[ 1 + \left( \frac{3B_2 Z^2 \lambda_r^2}{B_1 + B_2 Z^2 \lambda_r^3} \right) (\lambda_m - \lambda_r) \right] \quad (69)$$

Thus, if  $B_2 Z^2 \lambda_r^3$  is large compared to  $B_1$  the observed ratio will show a non-resonant linear-change with the incident wavelength  $\lambda_m$ .

The manganese data shown in Fig. 13 was corrected for the effect of Rayleigh scattering through the use of the equation:

$$\left[ \frac{R_e(\lambda_m)}{R_i(\lambda_m)} \right]_{\text{corrected}} = \frac{R_e(\lambda_m)}{R_i(\lambda_m)} \left[ 1 - B_3 (\lambda_m - \lambda_r) \right] ; B_3 = \frac{3B_2 Z^2}{B_1 + B_2 Z^2 \lambda_r^3} \quad (70)$$

The empirical value  $B_3 = 0.024/x\text{-units}$  was found from the slope of the observed base line. The ratio  $\left[ \frac{R_e(\lambda_m)}{R_i(\lambda_m)} \right]_{\text{corrected}}$  can be analyzed with Eq. 63 where  $\lambda_m = \lambda_r$  in the non-resonant terms.

REFERENCES

1. J. W. M. DuMond, *Ann. Rev. Nucl. Sci.* 8, 163 (1958).
2. D. E. Muller, H. C. Hoyt, D. J. Klein, and J. W. M. DuMond, *Phys. Rev.* 88, 775 (1957).
3. J. W. M. DuMond, *Rev. Sci. Instr.* 18, 626 (1947).
4. J. W. M. DuMond, D. A. Lind, and E. R. Cohen, *Rev. Sci. Instr.* 18, 617 (1947).
5. J. J. Murray, F. Boehm, P. Marmier and J. W. M. DuMond, *Phys. Rev.* 97, 1007 (1955).
6. M. E. Straumanis and E. Z. Aka, *J. Appl. Phys.* 23, 330 (1952); A. H. Compton and S. K. Allison, X-Ray in Theory and Experiment D. Van Nostrand Company, Inc., N. Y. (1947).
7. D. A. Lind, W. W. West, and J. W. M. DuMond, *Phys. Rev.* 77 475 (1950).
8. J. W. Knowles, *Can. J. Phys.* 37, 203 (1959); W. H. Zachariasen, Theory of X-Ray Diffraction in Crystals John Wiley & Sons, N. Y. (1946).
9. J. Berghuis, I. M. Haanappel, M. Potters, B. O. Loopstra, C. H. MacGillarry, and A. L. Veenendaal, *Acta. Cryst.* 8, 478 (1955).
10. W. F. Edwards, J. W. D. DuMond, and F. Boehm, *Nuclear Phys.* 26, 670 (1961).
11. W. F. Edwards, Ph.D. Thesis, California Institute of Technology, Pasadena, Calif., (1960).
12. K. Alder, A. Bohr, T. Huus, B. Mottelson, and A. Winther, *Revs. Modern Phys.* 28, 432 (1956).
13. F. R. Metzger, "Resonance Fluorescence in Nuclei" in O. R. Frisch (ed.), Progress in Nuclear Physics, Vol. 7, Pergamon, N. Y. (1959).
14. P. B. Moon and A. Storruste, *Proc. Phys. Soc. Lond.* A66, 585 (1953).
15. K. G. Malmfors, *Ark. Fys.* 6, 49 (1953).
16. F. R. Metzger, *J. Franklin Inst.* 261, 219 (1956).

17. R. L. Moessbauer, Z. Physik 151, 124 (1958).
18. H. Frauenfelder, The Moessbauer Effect, W. A. Benjamin, Inc., N. Y. (1962).
19. C. P. Swann and F. R. Metzger, Phys. Rev. 108, 982 (1957).
20. P. B. Smith and P. M. Endt, Phys. Rev. 110, 397 (1958); P. B. Smith and P. M. Endt, Phys. Rev. 110, 1442 (1958).
21. L. I. Schiff, Phys. Rev. 70, 761 (1946).
22. S. Devons, "The Measurement of Very Short Lifetimes" in Fay Ajzenberg-Selove (ed.), Nuclear Spectroscopy, Part A, Academic, N. Y. (1960).
23. F. D. Seward, Phys. Rev. 125, 335 (1962).
24. E. C. Booth, Nuclear Phys. 19, 426 (1960).
25. U. Fano, Nucleonics, 11 (8), 8 (1953).
26. R. D. Evans, The Atomic Nucleus, McGraw-Hill Book Company, Inc., N. Y. (1955).
27. J. M. Blatt, V. F. Weisskopf, Theoretical Nuclear Physics, John Wiley & Sons, N. Y. (1952).
28. W. E. Lamb, Jr., Phys. Rev. 55, 190 (1939).
29. K. S. Singwi and A. Sjolander, Phys. Rev. 120, 1093 (1960).
30. M. E. Rose, W. Miranker, P. Leak, L. Rosenthal, and J. K. Henrickson, "Westinghouse Atomic Power Division Report" SR-506, Vol. I and II (1954).
31. H. J. Lipkin, Annals of Physics 9, 332 (1960).
32. W. Heitler, The Quantum Theory of Radiation, Clarendon Press, Oxford (1954).
33. G. W. Grodstein, "X-Ray Attenuation Coefficients From 10 kev to 100 Mev" National Bureau of Standards Circular 583 (1957).
34. D. A. Lind, Ph.D. Thesis, California Institute of Technology (1948).
35. E. L. Chupp, J. W. M. DuMond, F. J. Gordon, R. C. Jopson, and Hans Mark, Phys. Rev. 112, 532 (1958).

36. J. Thirion, C. A. Barnes, C. C. Lauritsen, Phys. Rev. 94, 1076 (1954).
37. R. E. Holland and F. J. Lynch, Phys. Rev. 121, 1464 (1961).
38. G. M. Temmer and N. P. Heydenburg, Phys. Rev. 104, 967 (1956).
39. E. M. Bernstein and H. W. Lewis, Phys. Rev. 100, 1367 (1955).
40. J. W. M. DuMond, Ergeb, exakt, Naturw. XXVIII, 232 (1955).
41. E. A. Wolicki, R. Jastrow, and F. Brooks, "Calculated Efficiencies of NaI Crystals," NRL Report 4833.
42. L. C. Biedenharn and M. E. Rose, Revs. Modern Phys. 25, 729 (1953).
43. W. Franz, Z. Phys. 98, 314 (1935).
44. A. M. Bernstein and A. K. Mann, Phys. Rev. 110, 805 (1958).
45. P. P. Kane and G. M. Holzwarth, Phys. Rev. 122, 1579 (1961).